Tracing Carbonate Formation, Serpentinization, and Biological Materials With Micro-/Meso-Scale Infrared Imaging Spectroscopy in a Mars Analog System, Samail Ophiolite, Oman

Ellen K Leask, Bethany L Ehlmann, Rebecca N Greenberger, P.C. Pinet, Yves Daydou, Georges Ceuleneer, Peter Kelemen

Earth and Space Science

RESEARCH ARTICLE
10.1029/2021EA001637

Key Points:

- Meso-to micro-scale imaging spectroscopy identifies and maps carbonates, serpentine, and other hydrothermal phases in the Oman ophiolite
- Pigmentation from multiple types of biological materials including mats in travertine springs are distinguished even in shallow waters
- Detection thresholds of carbonate and serpentine when mixed can be >20area%, which has implications for interpretation of planetary data

Correspondence to:
E. K. Leask and B. L. Ehlmann,
ellen.leask@jhuapl.edu;
ehlmann@caltech.edu

Citation:
Leask, E. K., Ehlmann, B. L., Greenberger, R. N., Pinet, P., Daydou, Y., Ceuleneer, G., & Kelemen, P. (2021). Tracing carbonate formation, serpentinization, and biological materials with micro-/meso-scale infrared imaging spectroscopy in a Mars analog system, Samail Ophiolite, Oman. *Earth and Space Science*, *8*, e2021EA001637. https://doi.org/10.1029/2021EA001637

Received 3 JAN 2021
Accepted 20 SEP 2021

Tracing Carbonate Formation, Serpentinization, and Biological Materials With Micro-/Meso-Scale Infrared Imaging Spectroscopy in a Mars Analog System, Samail Ophiolite, Oman

Ellen K. Leask[1,2], Bethany L. Ehlmann[1,3], Rebecca N. Greenberger[1], Patrick Pinet[4], Yves Daydou[4], Georges Ceuleneer[5], and Peter Kelemen[6]

[1]Division of Geological & Planetary Sciences, California Institute of Technology, Pasadena, CA, USA, [2]Now at Johns Hopkins University/Applied Physics Laboratory, Laurel, MD, USA, [3]Jet Propulsion Laboratory, California Institute of Technology, Pasadena, CA, USA, [4]Institut de Recherche en Astrophysique et Planétologie (IRAP), Université de Toulouse, CNRS, UPS, CNES, Toulouse, France, [5]Geosciences Environnement Toulouse (GET), Université de Toulouse, CNRS, UPS, Toulouse, France, [6]Department of Earth & Environmental Sciences, Columbia University, Lamont Doherty Earth Observatory, Palisades, NY, USA

Abstract Visible-shortwave infrared (VSWIR) imaging spectrometers map composition remotely with spatial context, typically at many meters-scale from orbital and airborne data. Here, we evaluate VSWIR imaging spectroscopy capabilities at centimeters to sub-millimeter scale at the Samail Ophiolite, Oman, where mafic and ultramafic lithologies and their alteration products, including serpentine and carbonates, are exposed in a semi-arid environment, analogous to similar mineral associations observed from Mars orbit that will be explored by the Mars-2020 rover. At outcrop and hand specimen scales, VSWIR spectroscopy (a) identifies cross-cutting veins of calcite, dolomite, magnesite, serpentine, and chlorite that record pathways and time-order of multiple alteration events of changing fluid composition; (b) detects small-scale, partially altered remnant pyroxenes and localized epidote and prehnite that indicate protolith composition and temperatures and pressures of multiple generations of faulting and alteration, respectively; and (c) discriminates between spectrally similar carbonate and serpentine phases and carbonate solid solutions. In natural magnesite veins, minor amounts of ferrous iron can appear similar to olivine's strong 1-μm absorption, though no olivine is present. We also find that mineral identification for carbonate and serpentine in mixtures with each other is strongly scale- and texture-dependent; ~40 area% dolomite in mm-scale veins at one serpentinite outcrop and ~18 area% serpentine in a calcite-rich travertine outcrop are not discriminated until spatial scales <~1–2 cm/pixel. We found biological materials, for example bacterial mats versus vascular plants, are differentiated using wavelengths <1 μm while shortwave infrared wavelengths >1 μm are required to identify most organic materials and distinguish most mineral phases.

Plain Language Summary Imaging spectroscopy from airplanes or satellites helps us to map different rock types on Earth and other planets, using reflected visible to shortwave infrared light. With this technique, each pixel in an image has a corresponding spectrum in hundreds of wavelengths with absorptions that are fingerprints, diagnostic of specific material compositions. Here, we demonstrate how imaging spectroscopy can be used at smaller scales, in the field, in the lab, and on future rover and lander missions. We took an imaging spectrometer to the Samail Ophiolite (Oman), which has many of the same water-formed minerals and rock types as detected from orbit in some locales on Mars. We determined imaging spectroscopy can differentiate between minerals that look similar from distance and use the spatial context of mineral detections to understand the time order of events affecting a rock. Using an imaging spectrometer to find small pieces of unaltered rock left intact after fluids have transformed most of the rock reveals the pressure, temperature, and chemical environment during rock formation and later alteration. Rare minerals and unaltered relicts can then be sampled for intensive study. Plants and bacteria can also be mapped. Such capabilities are useful for environmental investigations on Earth and other planets.

1. Introduction

Reflectance imaging spectroscopy in the visible-shortwave infrared (VSWIR) wavelength range is a remote sensing technique that has been used to map compositional changes on a variety of planetary bodies, including Earth, Mars, Ceres, and Pluto (e.g., Bibring et al., 2005; Chabrillat et al., 2000; De Sanctis et al., 2015; Murchie et al., 2009; Pinet and Chevrel, 1990; Stern et al., 2015; Swayze et al., 1992). Prior geologic applications use the technique to detect and localize rare phases, distinguish mineral solid solutions and Fe (II)/Fe (III), and track subtle compositional changes, facilitating geologic interpretation. Imaging spectrometers are also now increasingly available for field use on Earth on unpiloted aerial vehicles (UAVs), tripod-based imaging systems, and mounted racks for laboratory scanning of samples (e.g., Greenberger et al., 2015). Imaging spectrometer instruments for in situ planetary exploration have also matured and been proposed for landed missions to make meso-scale landscape measurements from masts or micrometers-scale microscopic images when placed just above a surface or sample (e.g., Blaney et al., 2016; Ehlmann et al., 2016; Green et al., 2015; Pilorget and Bibring, 2013; Van Gorp et al., 2014).

Measurements of mineralogy with spatial context would be valuable for a surface mission to Mars and other planets. A handful of sites on Mars with both Mg carbonate and Mg serpentine have been identified from orbital data, including those in the vicinity of the Mars-2020 landing site at Jezero crater with its potential extended mission toward Nili Planum and Northeast Syrtis (Brown et al., 2020; Ehlmann & Mustard, 2012; Ehlmann et al., 2010; Michalski & Niles, 2010). These carbonate-serpentine sites are of particular interest, because such carbonate/serpentine systems on Earth host chemosynthetic life and produce abiotic hydrogen and methane gases (e.g., Rempfert et al., 2017; Schulte et al., 2006). Furthermore, serpentinization of ultramafic rocks can sequester carbon dioxide in carbonate minerals, removing it from the atmospheric and hydrologic reservoirs (e.g., Edwards and Ehlmann, 2015; Kelemen and Matter, 2008). On Mars, this removal of atmospheric carbon has been proposed as a possible mechanism for the planet's evolution from a robust surface hydrologic system (as evidenced by extensive fluvial systems, e.g., Carr, 1995; Hynek et al., 2010; Pieri, 1980) to the arid planet we see today (e.g., Edwards & Ehlmann, 2015; Pollack et al., 1987).

The large Samail ophiolite in Oman exposes serpentinized and carbonated ultramafic rocks at the Earth's surface in a semi-arid environment, with limited surface vegetation to obscure the underlying lithology, making it a Mars analog environment suited to investigation with imaging spectroscopy (e.g., Combe et al., 2006; Kelemen and Matter, 2008; Pinet et al., 2006; Roy et al., 2009). Here, we perform the first meso- and micro-scale field- and laboratory-based imaging spectroscopy of the Samail ophiolite to (a) understand the spectral diversity within natural carbonate/serpentine settings, (b) evaluate the capabilities of ground-based imaging spectrometers for targeting, sampling, and interpreting geological environments and environments hosting biological activity, and (c) consider lessons learned for detection and quantification of serpentine and carbonate in planetary datasets. We integrate data from 3 scales—airborne survey (Roy et al., 2009), outcrop imaging, and hand samples—to demonstrate how the micro- and meso-scale imaging help better interpret the larger scale mapping data by identifying endmember minerals, remnant protolith, and textural relationships between minerals indicative of process and/or timing, as well as the quantification of minerals and identification of biological materials at different scales. We also evaluate the detectability of key mineral phases, carbonate and serpentine, at these scales.

2. Methods

2.1. Field Site Geologic Setting

The Samail Ophiolite in Oman and U.A.E (Figure 1) is one of the largest and best preserved ophiolites on Earth. It is a fragment of Cretaceous oceanic lithosphere that formed in the Tethys Ocean ~96 Ma ago (Rioux et al., 2012). Its initial detachment in an intra-oceanic setting is virtually contemporaneous with its formation, that is in a mid-ocean spreading center setting (e.g., Boudier et al., 1985; Rioux et al., 2016), as its obduction on the Arabian continental margin started soon after and was completed before ~70 Ma ago (Glennie et al., 1973). The ophiolite exposes mafic to ultramafic rocks typical of the mantle and of the oceanic crust including mostly harzburgites, gabbros, dolerites and basalt (e.g., Hopson et al., 1981), less abundant dunites, wehrlites and pyroxenites, and rare tonalites-trondhjemites and chromitites (e.g., Amri et al., 1996; Braun & Kelemen, 2002; Boudier & Coleman, 1981; Clénet et al., 2010; Ceuleneer &

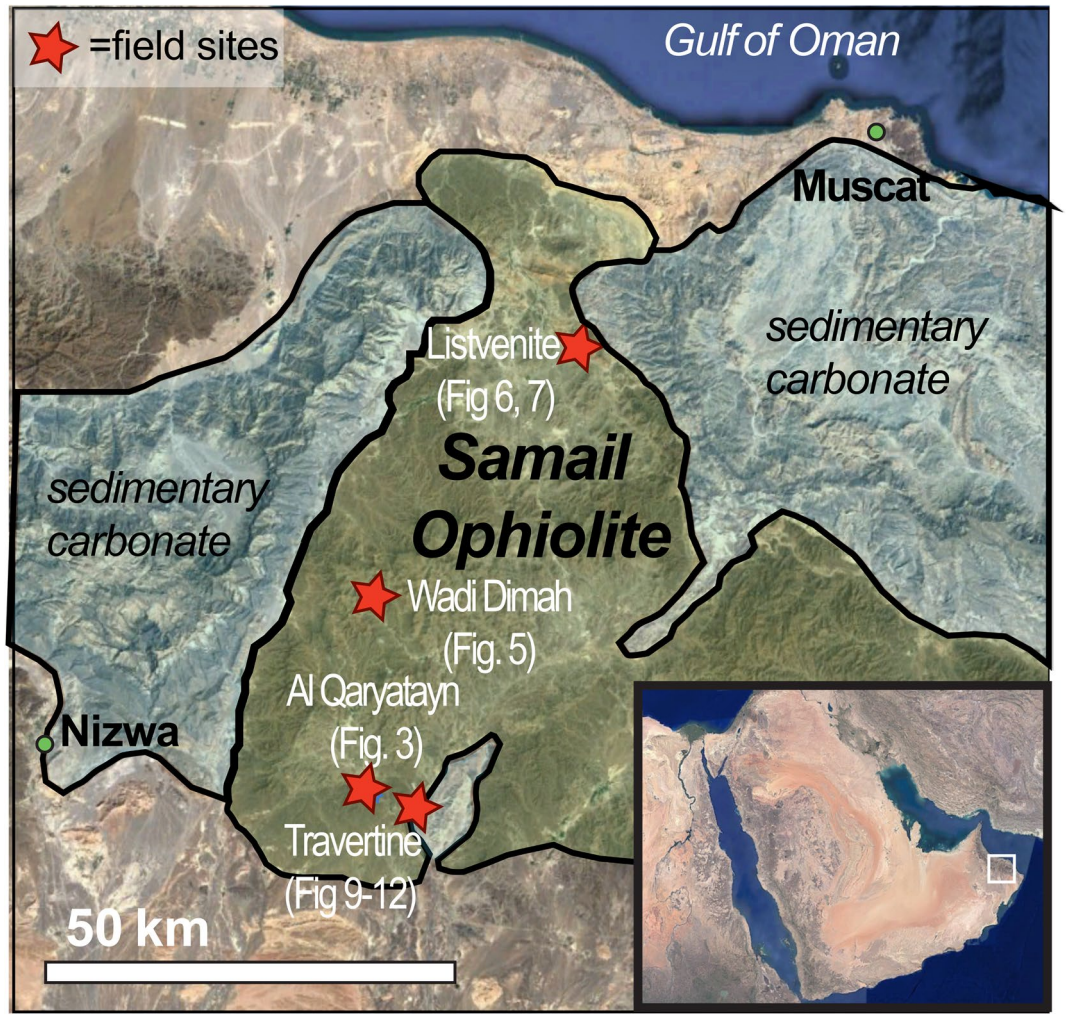

Figure 1. Field locations within the Samail Ophiolite, Oman. The Al Qaryatayn site (Figure 3) is a typical serpentinite with carbonate veins at many scales; the Wadi Dima site (Figure 5) contains a mixture of altered mafic and ultramafic rocks; the listvenite site (Figures 6 and 7) at the northern edge of the ophiolite reflects complete carbonation of the rock; and at the travertine site (Figures 9–12) at the southern edge of the ophiolite, hyperalkaline springs are actively precipitating carbonate on top of veined serpentinite.

Nicolas, 1985; Koga et al., 2001) . Ultramafic portions of the ophiolite are generally 40%–60% serpentinized (e.g., Dewandel et al., 2003; Hanghöj et al., 2010; Monnier et al., 2006), but locally have been more intensely serpentinized. The serpentinization history spanned a long period of time and covers a large spectrum of temperature and fluid compositions: it started in the mid-ocean ridge setting in response to hydrothermal seawater circulation (e.g., Gregory and Taylor, 1981; Rospabé et al., 2018) and continues today due to reaction with meteoric water (e.g., Barnes et al., 1978; Kelemen & Matter, 2008; Neal & Stanger, 1985). The most intensely serpentinized zones are typically found with associated carbonate, either in veins, or in travertine deposits at the surface. These travertine springs are often hyperalkaline, with pH of 10–12 (e.g., Canovas et al., 2017; Chavagnac et al., 2013; Neal and Stanger, 1984, 1985; Paukert et al., 2012). The subsurface and near-surface aquifers within these diverse lithologies are habitats that host an array of chemosynthetic life (Rempfert et al., 2017). Here, we investigate a range of sites within the ophiolite: two serpentinite sites with extensive veining (Al Qaryatayn and Wadi Dima); a listvenite site (complete carbonation of the ultramafic protolith, discussed below); and a travertine/serpentine site where groundwater springs come to the surface (Figure 1), subset from a wider set of acquisitions (e.g., Pinet et al., 2017). Three of these sites are within HyMap coverage (Figure 2), a pre-existing airborne imaging spectroscopy data set acquired over the ophiolite (Pinet et al., 2003).

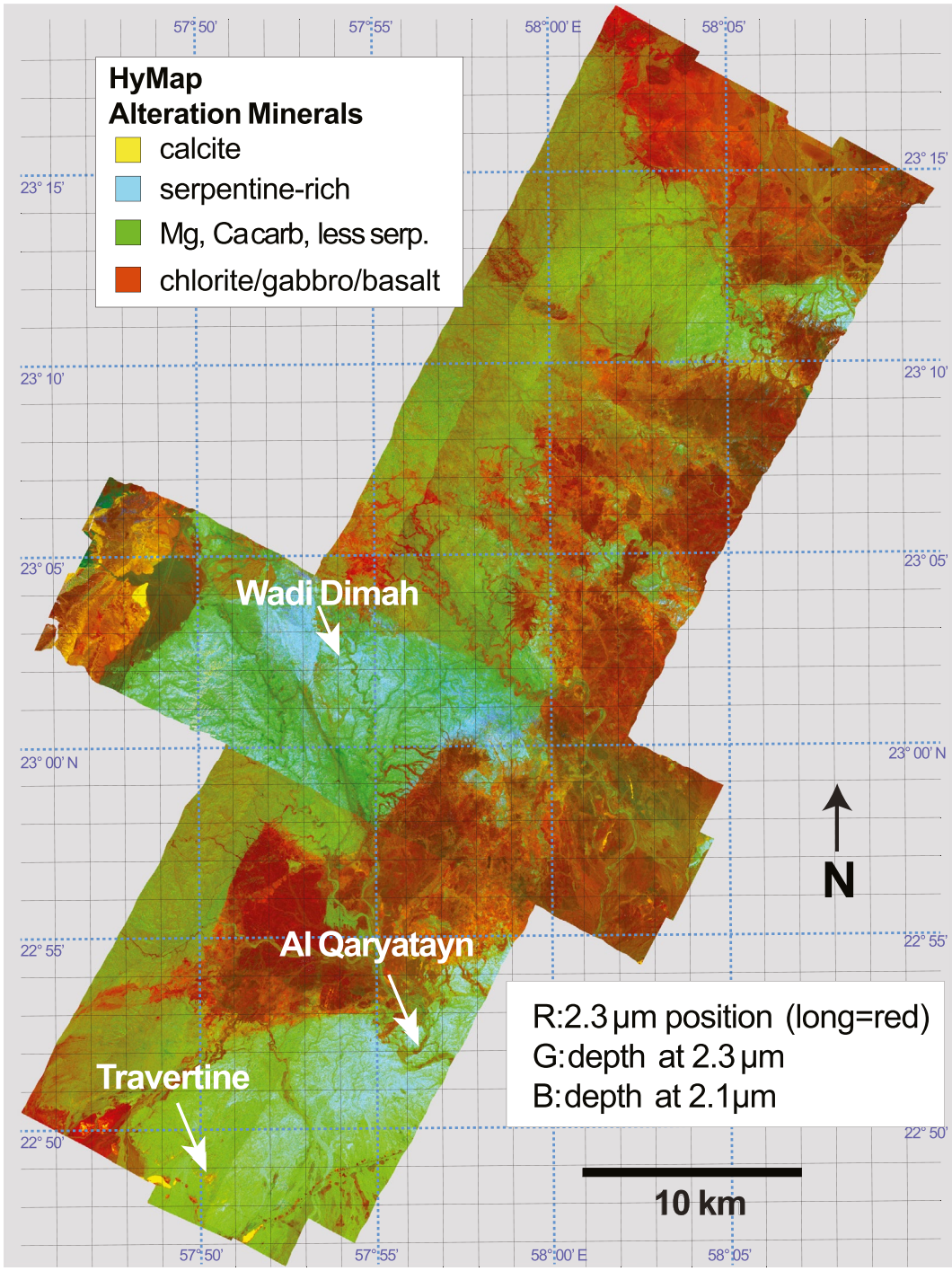

Figure 2. Context image of field site locations and ophiolite lithology. The qualitative HyMap color composite highlights compositional variability by assigning to red to the position of the absorption from 2.30 to 2.35 µm (longer wavelengths are redder), green is band depth at 2.3 µm, and blue is band depth at 2.12 µm. Ca-carbonate springs and limestones from the Hawasina group appear bright yellow. Green are Mg,Ca carbonates. The strongest Mg serpentine signatures are cyan. Reds are consistent with chlorite/gabbro/basalt compositions.

2.2. Imaging Spectroscopy

The pushbroom imaging spectrometer used for this work was custom-built by Headwall Photonics, Inc. for Caltech, and combines data from two sensors to cover a spectral range from ~0.4–2.6 μm with a signal-to-noise ratio above 100 in all channels with laboratory illumination. The VNIR sensor (visible-near infrared) measures wavelengths 0.4–1.0 μm with 5-nm spectral resolution, while the SWIR sensor (shortwave-infrared) covers the ~1.0–2.6 μm region with 6-nm spectral resolution (see Greenberger et al., 2016 for further detail). At a standoff distance of 20 m, the instantaneous field of view (IFOV) is 0.6 cm in VNIR wavelengths and 1.7 cm in SWIR. In the laboratory at a standoff of ~20 cm, the IFOVs are ~70 μm/pixel and ~210 μm/pixel, respectively. The spectrometer is mounted on a rotating stage on a tripod in the field, or above a linear sample stage in the laboratory, and takes ~30 s to ~3 min to acquire a single image, depending on extent of the image swath and integration time. The VNIR and SWIR arrays gather data simultaneously. Data are calibrated to Spectralon panels of known reflectance that are placed in the scene. Panels of 5%, 20%, and 99% were utilized in our fieldwork. (Note that a landed planetary mission would instead use an onboard calibration target on the craft.) For this work, we co-register the two images and then down-sample and resample the spatial resolution of the VNIR sensor to match the lower spatial resolution SWIR array, matching the SWIR to the VNIR spectrum at 0.969 μm through a multiplicative scaling. Hand samples were cut to provide a flat surface for imaging in the laboratory to ensure that the entire image was in focus (see Leask & Ehlmann, 2016), but no other preparation was involved.

2.2.1. Field Data Calibration and Atmospheric Correction

Field data were calibrated to reflectance by subtraction of dark current, measured at the time of observation, and division by a flat-field correction, obtained by laboratory measurement of an integrating sphere, to account for non-uniform spectral instrument response on the detector pixel elements. Examination of results shows a small amount of spatial striping from differential detector pixel sensitivity persists, but this does not obscure maps in further analysis. We used an empirical method for atmospheric correction: first a dark-object subtraction (Chavez, 1988) to remove the additive aerosol-scattering component, followed by multiplicative correction derived by a wavelength-dependent scalar between the 99% reflectance Spectralon panel in each scene and laboratory spectra of the panel. The formula for correction of each scene image cube pixel element is shown in the equations below where i is the spatial dimension corresponding to the detector spatial dimension, k is the spectral dimension corresponding to the detector spectral dimension, and the middle index (j, letter not used), is the spatial dimension of the image obtained by the pushbroom motion scan.

$$\text{Corrected Scene}_{i,*,k} = \frac{\text{RawScene}_{i,*,k} - \text{Dark}_{i,k}}{\text{Flat Field}_{i,k}} \tag{1}$$

$$\text{Reflectance}_{i,*,k} = \left(\text{CorrectedScene}_{i,*,k} - \text{CorrectedSceneDarkObject}_{k}\right) * \frac{\text{LabSpectralon}_{k}}{\left(\text{SceneSpectralon}_{k} - \text{CorrectedSceneDarkObject}_{k}\right)} \tag{2}$$

Comparison of data from darker calibration panels in the scene to their laboratory spectra were used as a check on the success of the approach. In our data, the atmospheric path length in a single image could range from ~1 m to >500 m (mountains in the distance) with many of the atmospheric bands completely saturated, making radiative transfer modeling difficult. Additionally, the aspects of facets of an outcrop vary such that phase-angle dependent scattering induces pixel-to-pixel variations in atmospheric absorptions; however, our data set did not collect digital models of surface topography to obtain facet orientations (e.g., Jakob et al., 2017). Consequently, in figures of field data spectra shown below, wavelengths of atmospheric oxygen and water absorptions are made partially opaque because of residual atmospheric features (at ~0.76 μm, ~1.15 μm, and broad bands at ~1.4 and ~1.9 μm). Furthermore, the longest wavelengths >~2.5 μm of the SWIR were not always reliable in the field data set, likely resulting from decreased detector sensitivity at the longest wavelengths and the low signal at this part of the spectral range due to absorptions by atmospheric water beyond 2.5 μm.

The outcrop data have facets where portions of the rock have different orientation relative to the sun. Orientation/viewing geometry has a multiplicative effect, the cosine of the solar incidence angle, on the spectra. By using parameters such as band depths, this multiplicative factor cancels out, and we can map minerals without orientation effects except for the phase-dependent atmospheric effects described above.

Table 1
Relevant Minerals, Their Chemical Formulae, and Diagnostic Absorption Features Used in Detection and Mapping; for Mineral Indicator Parameterization See Tables A1 and A2

Materials investigated[a]	Formulae	Diagnostic absorptions (μm)	(References)
Carbonates			
Calcite	$CaCO_3$	(2.17 sometimes), 2.33–2.34, 2.53–2.54	Gaffey (1985); Gaffey (1986)
Dolomite	$CaMg(CO_3)_2$	2.315–2.325, 2.51–2.52	Gaffey (1985); Gaffey (1986)
Magnesite	$MgCO_3$	2.30–2.31, 2.50	Gaffey (1985)
Siderite	$Fe^{2+}CO_3$	1.1, 2.32–2.33, 2.53	Gaffey (1985)
Igneous minerals			
Olivine (forsterite, fayalite)	$(Mg, Fe^{2+})_2SiO_4$	~0.85, 1.05, 1.25	Sunshine and Pieters (1998)
Orthopyroxene (enstatite, ferrosilite)	$(Mg, Fe^{2+})_2Si_2O_6$	~0.9, ~1.9	Cloutis and Gaffey (1991)
Clinopyroxene (e.g., augite, diopside)	$Ca(Fe^{2+}, Mg)\ Si_2O_6$	~1.05, ~2.3	Cloutis and Gaffey (1991)
Plagioclase (e.g., anorthite)	$CaAl_2Si_2O_8$	(no strong features, especially in mixtures)	
Secondary silicate minerals			
Serpentine	$(Fe^{2+}, Mg)_3Si_2O_5(OH)_4$	~1.4, 2.12, 2.32–2.34, 2.5	King and Clark (1989); Bishop et al. (2008)
Chlorite (clinochlore, chamosite)	$(Mg, Fe^{2+})_5Al(AlSi_3O_{10})(OH)_8$	1.39, 2.25, 2.33–2.35	King and Clark (1989); Bishop et al. (2008)
Prehnite	$Ca_2Al_2Si_3O_{10}(OH)_2$	1.48, 2.23 + 2.29, 2.34	White et al. (2017)
Epidote	$(Ca_2)(Al_2Fe^{3+})Si_2O_7(SiO_4)O(OH)$	1.56, 2.25, 2.34	White et al. (2017)
Mica (Cr-muscovite/fuchsite)	$K(Al,Cr)_3Si_3O_{10}(OH)_2$	1.4, 2.20–2.25, 2.30–2.35	Bishop et al. (2008) (for other micas)
Kaolinite	$Al_2(Si_2O_5)(OH)_4$	1.41, 2.17 + 2.21	Bishop et al. (2008)
Quartz	SiO_2	(none)	

[a]There are also primary and secondary oxides in the ophiolite (e.g., magnetite, chromite, hematite, and goethite), some of which have characteristic electronic absorptions that are detectable at the VSWIR wavelengths, but these phases were not a focus of systematic investigation in this study. Talc and smectite were searched for and not found (as also in Leask & Ehlmann, 2016).

2.2.2. Spectral Parameters and Mineral Mapping

Table 1 summarizes minerals of interest to this study and their chemical formulae, and many of these minerals can be detected from their spectroscopic features. The spectral features are electronic transitions or molecular vibrations characteristic of specific minerals, atmospheric gases, water, or biological materials. A series of parameters were developed to distinguish minerals and other materials based on their major absorptions, exact band centers of those absorptions, and slopes/ratios where only part of the absorption was covered (Table 2; after Greenberger et al., 2020; Pelkey et al., 2007; Viviano-Beck et al., 2014). Parameters were then aggregated with thresholds highlighting the presence and/or absence of diagnostic features to map key materials within the image (Table 3).

Detailed discussion of scene material characterization and parametrization is discussed with each relevant field locality in Section 3. In brief, threshold and parameters were first used to mask shadows, clouds, sky, and vegetation are given in Table 3 under "Masks." We mask scene locations with reflectance <0.05 at 1.0 and 1.5 μm (typically shadowed regions) as well as locations with absorption features at 1.13 and 1.455 μm >0.1 (clouds and sky). In figures where we focus on mineralogy, we also mask out biological materials, primarily small bushes.

Mineral maps were developed using combinations of parameters (Tables 2–3). For a given mineral, we combine parameters capturing the diagnostic absorptions (Table 1) not masked by atmospheric bands; for example, Mg serpentine has a 2.12-μm absorption in addition to a deep 2.32-μm absorption. In cases where our parameters may capture spectrally similar minerals, we also explicitly exclude pixels with additional absorptions—for instance, epidote and chlorite both have absorptions at 2.25 and 2.34 μm, but epidote

Table 2
Spectral Parameters, Formulae, and the Phase(s) Indicated by the Parameter

Parameter	Formula (wavelengths in μm)[a]	Notes
BD680	1-R0.68/Continuum (0.613 to 0.740)	Organics, will also identify certain Fe-oxides/oxyhydroxides
R800/R500	R800/R500	High in dry vegetation
R1000	R1000	Reflectance/dark
R1070	R1070	Reflectance/albedo
R1070/R1650	R1070/R1650	Water (empirical for SWIR channel: nearly zero IR reflectance of water at 1650)
BD1130_atmos	1-R1.130/Continuum (1.065 to 1.170)	Atmosphere
BD1200_org	1-R1.200/Continuum (1.090 to 1.245)	Organics
BD1450_broad	1-R1.450/Continuum (1.31 to 1.67)	Hydration; absent in pyroxene
BD1455_broad	1-R1.455/Continuum (1.405 to 1.505)	Atmosphere/water
R1457/R1480	R1457/R1480	Prehnite
BD1475_prehnite	1-R1.475/Continuum (1.455 to 1.510)	Prehnite OH
R1500	R1500	Reflectance/dark
R1500/R1000_fe_slope	R1500/R1000	Fe-slope (e.g., pyroxene, olivine, serpentine)
R1500/R2400	R1500/R2400	Pyroxene shape (also has many false positives)
BD1565_epidote	1-R1.565/Continuum (1.490 to 1.655)	Epidote
BD1725	1-R1.725/Continuum (1.640 to 1.785)	Organics
R1750/R2120	R1750/R2120	Dry vegetation
BD2120	1-R2.116/Continuum (2.065 to 2.185)	Boxy ~2.1-μm absorption in Mg serpentine
BD2120_2	1-R2.110/Continuum (2.080 to 2.160)	Boxy ~2.1-μm absorption in Mg serpentine
R2165/R2110	R2165/R2110	Serpentine, organics
BD2180_kln	1-R2.18/Continuum (2.1 to 2.24)	Part of kaolinite doublet
BD2200_broad	1-R2.20/Continuum (2.15 to 2.30)	Si-OH, (illite/muscovite)
BD2200_kln	1-R2.21/Continuum (2.1 to 2.24)	Part of kaolinite doublet
Kaolinite_slope	(R2.232 + R2.238)/(R2.202 + R2.208)	Positive slope at long end of kaolinite doublet to distinguish from Si-OH or other overlapping features
BD2230	1-R2.230/Continuum (2.15 to 2.27)	Si-OH; prehnite
BD2250	1-R2.25/Continuum (2.18 to 2.265)	AlFe-OH or Si-OH; chlorite
BD2255	1-R2.255/Continuum (2.10 to 2.43)	Epidote
BD2300_carb	1-R2.30/Continuum (2.16 to 2.34)	2.3- μm absorption in Mg-carbonates
BD2320	1-R2.318/Continuum (2.120 to 2.37)	Dolomite, serpentine
BD2320_2	1-R2.322/Continuum (2.29 to 2.358)	Dolomite, serpentine
BD2340	1-R2.34/Continuum (2.18 to 2.39)	C-O combination in carbonates; wavelengths optimized for calcite; prehnite; epidote
BD2340_narrow	1-R1.234/Continuum (2.286 to 2.352)	C-O combination in carbonates; wavelengths optimized for calcite
BD2340_compare	1-R1.234/Continuum (2.120 to 2.370)	C-O combination in carbonates; continuum wavelengths identical to BD2320 to distinguish calcite from dolomite
BD2350	1-R2.350/Continuum (2.160 to 2.385)	Chlorite
BD2360	1-R2.358/Continuum (2.29 to 2.40)	Illite/muscovite
BD2390	1-R2.386/Continuum (2.35 to 2.42)	Talc

Table 2
Continued

Parameter	Formula (wavelengths in μm)[a]	Notes
D2500	1-R2.47/R2.40	Drop in carbonates at 2.5 μm due to absorption
NDVI	(R0.85-R0.65)/(R0.85 + R0.65)	Chlorophyll

[a]R, reflectance at that wavelength; Continuum (# to #) = the value of a straight line continuum between these points at the wavelength of the numerator.

has an additional diagnostic absorption at 1.56 μm, while chlorite has an additional absorption at 1.39 μm. Carbonates are identified based on the similar depths (within ~25%) of 2.3-μm and 2.5-μm absorptions (partially characterized by a "peak" at ~2.4 μm and downturn toward 2.5 μm in the field data because the 2.5 μm carbonate absorption is obscured by atmospheric absorptions). The center wavelengths of the minima of these absorptions can be used to distinguish between carbonate minerals (Table 1). Mg serpentines are differentiated from carbonates by their 2.12-μm absorption and–where data quality allows–asymmetry in the large 2.32-μm and shallow 2.5-μm absorptions. Note that evidence for amphiboles (actinolite-tremolite) and brucite was searched for in the hyperspectral image data but not identified. We do not include oxides in this study because chromite and magnetite formed during serpentinization darken rocks but do not yield distinctive, detectable spectral features in this wavelength range. Goethite and other ferric oxides are observed in visible/near-infrared spectra and are surface weathering patinas on these rocks but are not a main focus of this work.

The mineral occurrence classification maps of Section 3 were constructed via automated methods after manual inspection of the spectra from select individual pixels to understand the spectral variability in each scene. As such, this was executed as a semi-quantitative process, dependent on expert user classification to produce areal maps of mineral occurrence on a per-pixel basis. Thresholds for parameter combinations leading to classification of a pixel as hosting a particular mineral were determined by setting an initial minimum threshold and adjusting iteratively up or down after checks that the spectral properties of pixels matched their classified mineral designation. Thresholds for parameter combinations leading to classification of a pixel as hosting a particular mineral are given in Table 3. Mixed pixels with the spectral properties of many phases or ambiguous spectral properties were classified according to Table 3 and were either assigned the spectrally dominant mineralogy or not assigned a discrete mineral occurrence classification, leading to a substantial population of unclassified pixels in figures of the field data.

2.2.3. Secondary Mineral Detection and Area% Occurrence Quantification

Ideally, abundance estimation in weight% or volume% would be obtained via per-pixel nonlinear unmixing with radiative transfer models (e.g., Hapke, 1981; Lapôtre et al., 2017; Mustard & Pieters, 1989; Shkuratov et al., 1999), but for 1–15 GB scenes or larger with >1 million independent spectra and over a dozen endmembers, use of such algorithms is computationally prohibitive. Additionally, because of inherent variability in spectral properties of each of the compositional endmembers due to solid solution, even with sufficient computing, more sophisticated non-linear techniques for meso-scale quantification are not straightforward. We initially tried a linear unmixing code based on Heylen et al. (2011) but found that it did not reliably discriminate between serpentine and different carbonates in mixtures. Best-fit solutions typically matched the brightnesses of given endmembers, rather than absorptions, and the brightness of the region of interest varies greatly due to changing roughness, changing viewing angles across an outcrop with shadows, and patinas of iron oxides. Consequently, for this initial work, we use the simple areal percentage (number of pixels) with an unambiguous occurrence of a phase, as captured by the parameters, to evaluate composition and compositional variation across field sites. That is, each pixel in a scene was classified as a single spectrally dominant mineral according to combinations of parameters as described in Table 3 or was left unclassified as a mixture.

Estimation of abundance using area% occurrence works reasonably well at the micro-scale (<1 mm) where indeed most pixels do encompass a single phase (see also Leask & Ehlmann, 2016 for comparison with x-ray diffraction mineralogy). Such an approach is very unlikely to yield good estimates of abundance at many meters-scale from airborne/orbital spatial scales but does still provide information on mineral occurrence and relative prevalence. At the meso-scale (mm to cm), area% occurrence, that is, reporting unambiguous

Table 3
Formulas and Thresholds Used for Mineral Classification and Masking of Other Materials Typically Used in Field Imaging Spectroscopy Data Mapping

Material	Spectral feature(s) present	Spectral feature(s), material(s) absent
Masks		
Shadows	R1000 < 0.05 R1500 < 0.05	
Clouds and sky	BD1130_atmos >0.1 BD1455_broad >0.1	
Vegetation and water	BD1200_org >0.02 R1070/R1650 > 1.05 BD1455_broad >0.1	
Dry vegetation	R2165/R2110 > 1.05 R1750/R2120 > 1.05 BD1455_broad >0.1	
Field mask	Shadows –OR– Clouds and sky –OR–Vegetation and water –OR–Dead vegetation	
Minerals		
Pyroxene	R1500/R1000 > 1.5 R1500/R2400 > 1.5	BD1450broad <0.02 D2500 < 0.002 Field mask
Calcite	BD2320_2 > 0.005 BD2340 > 0.005 max (BD2340, BD2340_narrow, BD2340_compare) > BD2320 BD2340 > BD2300_carb D2500 > 0 D2500/BD2320 > 0.75	BD2120 < 0.01 BD2390 < 0.03 BD1725 < 0.1 Field mask
Chlorite	BD2250 > 0.002 BD2350 > 0	BD1475_prehnite <0.005 BD1565_epidote <0.005 Field mask
Dolomite	BD2320 > 0.005 BD2320_2 > 0.005 BD2320 > max (BD2340, BD2340_narrow, BD2340_compare) BD2320 > BD2300_carb D2500 > 0 D2500/BD2320 > 0.45	BD2120 < 0.01 BD2390 < 0.03 BD1725 < 0.1 Field mask
Fe-dolomite	R1500/R1000_fe_slope >1.2 BD2320 > 0.005 BD2320_2 > 0.005 BD2320 > max (BD2340, BD2340_narrow, BD2340_compare) BD2320 > BD2300_carb D2500 > 0 D2500/BD2320 > 0.45	BD2120 < 0.01 BD2390 < 0.03 BD1725 < 0.1 Field mask
Epidote	BD1565_epidote >0.015 BD2255 > 0 BD2340 > 0	Field mask
Illite/Cr-muscovite	BD2360 > 0 BD2200_broad >0	Field mask
Kaolinite	BD2180_kln >0 BD2200_kln >0 Kaolinite_Slope >1	Field mask
Magnesite	BD2300_carb >0.005 BD2300_carb > max (BD2340, BD2340_narrow, BD2340_compare) BD2300_carb > BD2320 D2500 > 0 D2500/BD2320 > 0.75	BD2120 < 0.01 BD2390 < 0.03 BD1725 < 0.1 Field mask
Fe-Magnesite	R1500/R1000_fe_slope >1.2 BD2300_carb >0.005 BD2300_carb > max (BD2340, BD2340_narrow, BD2340_compare) BD2300_carb > BD2320 D2500 > 0 D2500/BD2320 > 0.75	BD2120 < 0.01 BD2390 < 0.03 BD1725 < 0.1 Field mask
Prehnite	BD1475_prehnite >0.005 BD2340 > 0 R1457/R1480 > 1 BD2230 > 0.005	Field mask
Serpentine	BD2120_2 > 0.005 BD2320 > 0.005 R2165/R2110 > 1	Field mask
Strong serpentine	R1500 > 0.2 BD2120_2 > 0.04 BD2320 > 0.15 R2165/R2110 > 1	Field mask

detections of occurrences in polymineralic assemblages, is a useful first-order approximation for assessing compositional variation that can be informative. This is particularly true at this field site where secondary alteration exhibits zoning, dominated by certain minerals at cm-to mm-scales. Discussion of detection thresholds for different minerals for area% occurrence and evaluation of their dependence on the spatial scale of mixing is further detailed in section 4.3.

2.3. HyMap Data

Field locations in this study were chosen with particularly strong carbonate and serpentine spectral signatures in the HyMap data set, processed in earlier investigations (e.g., Clenet et al., 2013; Roy et al., 2009; Figure 2). Airborne hyperspectral data for this region were acquired in December 2002, using the HyMap instrument, collected data between 0.45 and 2.48 μm, with a spectral resolution of 15–20 nm and a spatial sampling of 12 m/pixel (Cocks et al., 1998; Combe et al., 2006; Pinet et al., 2003; Roy et al., 2009). The data were atmospherically corrected with a radiative transfer model and geometrically corrected using a digital elevation model (for further detail, see Clenet et al., 2013). Spectra at HyMap's large spatial scale over the field sites were extracted for comparison.

2.4. X-Ray Diffraction and Independent Compositional Analysis

A previous publication (Leask & Ehlmann, 2016) investigated the relationship between areal mapping of mineral abundance with microimaging infrared spectroscopy and estimates derived from X-ray diffraction (XRD) patterns and energy-dispersive spectroscopy (EDS) areal maps from chemistry. For most samples, the techniques agree in abundance estimates to within 10% for serpentine and carbonate phases. For this study, XRD patterns were measured for only select samples on a PANalytical X'Pert Pro instrument at the California Institute of Technology, which has a Cu K-alpha radiation source. We analyzed a 2θ range from 20 to 60°, using a current of 40 mA, voltage of 45 kV, and time step of 80 s.

2.5. Spectral and Pattern Libraries

VSWIR reference spectra shown are from the United States Geological Survey's Spectral Library (version 7; Kokaly et al., 2017) or from Brown University's Reflectance Experiment Laboratory (RELAB) database, resampled to the same spectral wavelengths as our data set. Reference XRD patterns were downloaded from RRUFF (Bindi et al., 2015).

3. Results

We focus on four sites that encompass four different geologic settings within the ophiolite and thus the types of geological and biological investigations enabled by imaging spectroscopy (Figure 1). The Al Qaryatayn site is a typical ultramafic serpentinite site, with carbonate veins at sub-mm to cm-scale, while Wadi Dima contains both mafic and ultramafic altered rocks. The listvenite site at the northern edge of the ophiolite is heavily metasomatized as part of the basal sequence of the ophiolite (e.g., Falk & Kelemen, 2015). At the southern edge of the ophiolite, we imaged a hyperalkaline travertine spring, where calcite is actively precipitating on top of veined serpentinite.

3.1. Al Qaryatayn (22.870 N, 57.939 E)

This outcrop is a heavily veined serpentinite exposed above a dry valley. At a measurement standoff distance of ~30 m, the spectral signatures are dominated by Mg serpentine (Figures 3a and 3b), with a weak 2.12-μm absorption, and a strong 2.33-μm absorption coupled with a downturn toward what we infer to be a smaller 2.5-μm absorption (these absorptions are combinations and overtones of Mg-OH vibrations; Bishop et al., 2008; King and Clark, 1989). The sole variation is in the strength of these serpentine-related absorptions (Figures 3g and 3h). However, imaging the same outcrop at a distance of ~2.5 m (Figures 3c and 3d), carbonate veins ~1–5 cm thick are clearly distinguished by their bright white color, presence of a 2.3-μm absorption coupled with a downturn toward an inferred strong 2.5-μm absorption, and the lack of 2.12-μm serpentine absorption. The data quality of the 2.4–2.6 μm wavelength range is poor, so we cannot measure the expected band center at ~2.5 μm. Instead, we look at the width and position of the "peak" between the 2.3 and 2.5 μm absorptions, and the slope between 2.38 and 2.45 μm, to infer the "strength" of the inferred 2.5- μm absorption feature from the slope of the downturn. Within the observed area, we see the band centers of the absorptions shift from ~2.315–2.320 μm, consistent with dolomite (Gaffey, 1986) or serpentine, to ~2.330–2.340 μm, consistent with calcite. At 2.5-m standoff, a minimum of ~22% (58,539/266,817) of the pixels in the image are classified as carbonate veins, dominantly dolomite or calcite. Unclassified pixels, approximately one-third of the image, are those with weaker absorptions or strengths not uniquely characteristic of one mineral: they are mixtures of phases.

In the laboratory, we cut open a typical example of the fine-grained serpentinized rock from this site and imaged it at ~250 μm/pixel scale (Figures 3e and 3f). Millimeter-scale carbonate veins within a matrix of serpentine are readily visible at this scale, accounting for at least an additional ~22 area% (6,717/30,010) of this rock. If we assume this example is typical of the whole outcrop, this means that an outcrop that qualitatively appears to be entirely Mg serpentine from a distance of 30-m actually contains ~40% carbonate veins (22% plus an additional 22% of the remaining ~78% matrix) at multiple scales. In Figure 4, we use serpentine and calcite spectral endmembers from this sample to investigate linear mixtures. The 2.5-μm carbonate absorption becomes identifiable at 30%–40% calcite. The diagnostic 2.12-μm minimum of serpentine

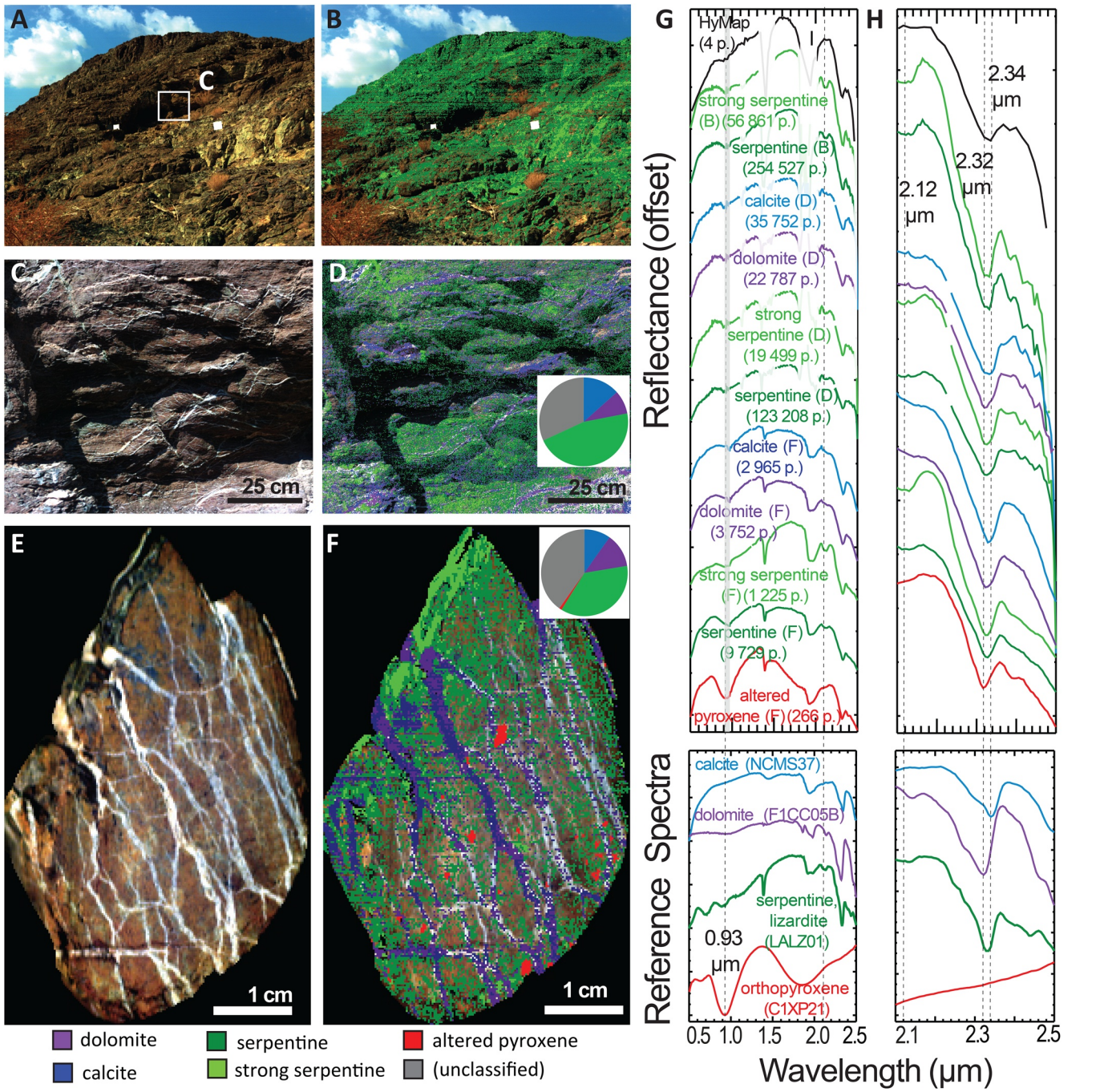

Figure 3. Al Qaryatayn field site serpentinite with carbonate veins at multiple scales. (a and b) Outcrop overview taken from a distance of ~20–40 m. White squares are 30 × 30 cm Spectralon panels; reddish-brown areas in the parameter map are bushes. Green colors in (b) map pixels classified as serpentine, based on parameters. (c and d) Close-up image of the veined serpentinite. At this scale, veins are mapped as a mixture of calcite and dolomite and account for ~22 area% of the pixels in the scene at meso-scale. (e and f) Hand sample of typical matrix from this site shows further mm-scale carbonate veining at smaller scales of both calcite and dolomite (accounting for ~22% of the rock matrix at micro-scale), a cross-cutting coarse serpentine vein, and small, partially altered, remnant orthopyroxenes. Mineral maps are overlain on the sample at (f). (g, h) Spectra corresponding to the parameter maps in panels (b, d, f) with the number of pixels used in spectral averages from a region of interest tracing the composition. Colors of spectra correspond to colors in the parameter maps. Gray line at 0.97 µm obscures the detector join, while bands of low atmospheric transmission are transparent in field data. Detail from the key 2.1–2.5 µm region is shown in (h). Pie charts were produced on a per pixel basis for that scale. Unclassified pixels are transparent in (b, d, f) classification maps and gray in the pie charts.

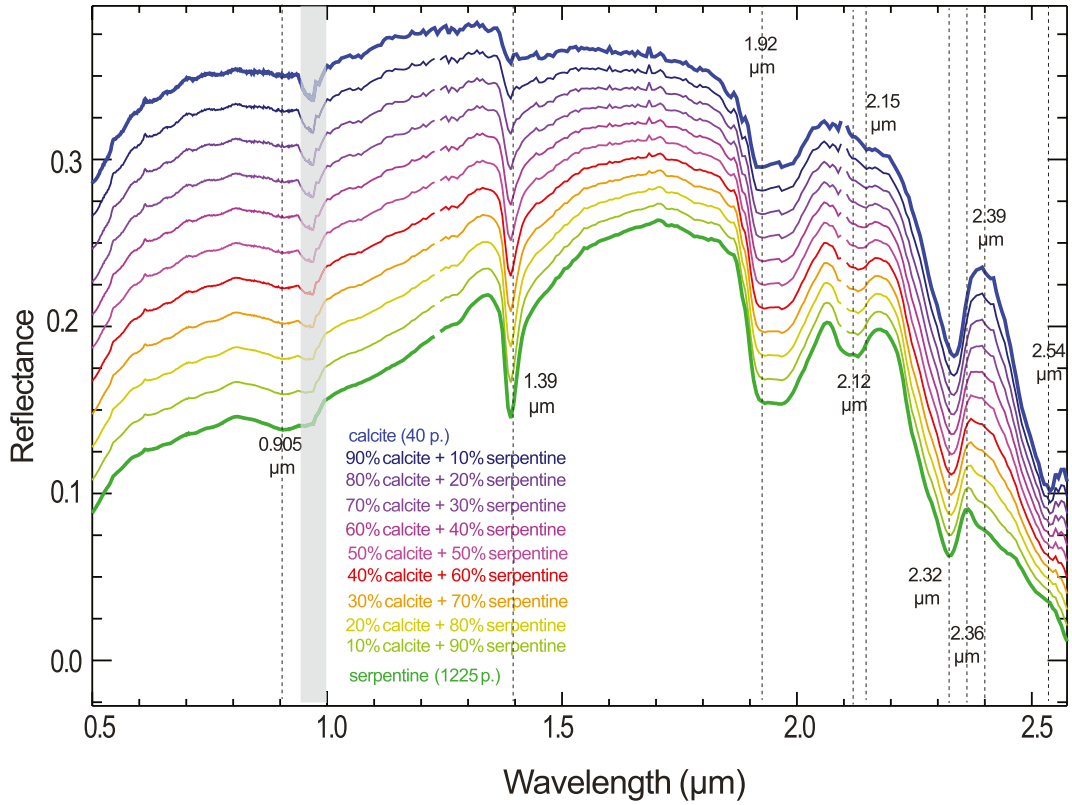

Figure 4. Computed linear mixtures between serpentine and calcite (endmember spectra from Al Qaryatayn hand sample imaged in the laboratory (Figures 3e and 3f). The diagnostic Mg serpentine absorption minimum at 2.12 μm disappears at about 30% calcite/70% serpentine; here, the longer-wavelength uptick defining the 2.54-μm calcite absorption also becomes distinguishable in high quality data. The "peak" at ~2.4 μm (between 2.3 and 2.5 μm absorptions) takes on a broader shape at ~ 50% serpentine/calcite. The gray bar is a spectral region where data are suspect, due to lower calibration accuracy proximal to the short and long wavelength spectrometer joins.

(see Section 4.2.2.) disappears after addition of just ~30% calcite, leaving only the 2.15-μm minimum of carbonate, highlighting the challenge of unique serpentine discrimination in a mixture with carbonate.

We also observe several interesting petrographic textures at the lab scale, including small zones of partially altered orthopyroxene (Figures 3e and 3f). Pyroxenes have broad electronic absorptions (due to Fe^{2+}) at ~1 and 2 μm (e.g., Hunt et al., 1970). The exact position of these absorption features changes with pyroxene composition, with orthopyroxene bands usually centered ~0.9 and 1.9 μm and clinopyroxenes centered ~1.05 and 2.35 μm, with some variability (e.g., Cloutis & Gaffey, 1991); here, the band centers at 0.93 μm indicate an orthopyroxene.

A large vein of coarse crystalline serpentine cross-cuts several smaller carbonate veins at the top left edge of the sample (Figure 3f), indicating that the rock underwent a later stage of serpentine veining after the initial formation of carbonate veins, and that the fluids in this later stage were significantly more enriched in silica or contained less CO_2. Distinct zones of calcite and dolomite within the same carbonate veins likely mean that the fluid composition changed over the course of carbonate vein formation. Dolomite tends to be found near the center of larger calcite veins, where we would expect the last fluid to flow.

3.2. Wadi Dima (23.044 N, 57.900 E)

This site is a veined serpentinite outcrop at the bottom of a dry valley (Figure 5). Nearby, we see a small exposure of layered pyroxene/plagioclase cumulates, indicating a more calcium- and aluminum-rich protolith in this region. With the imaging spectrometer we can track veins, fractures, and alteration of a variety of compositions. Averaged, the spectrum of the whole outcrop is consistent with being serpentine-dominated.

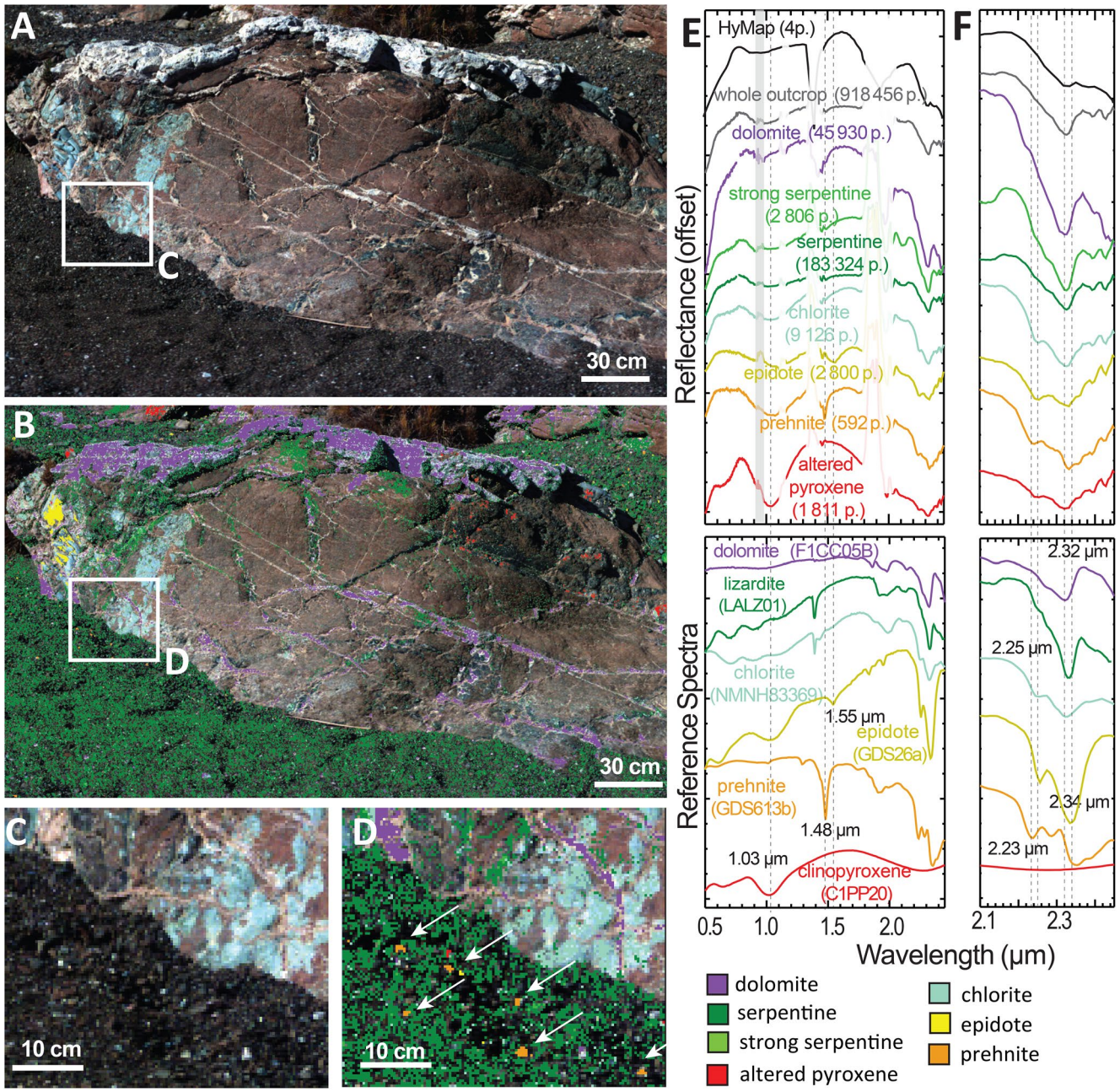

Figure 5. Wadi Dima field site, showing typical carbonate/serpentine mineralization in addition to a number of low-grade metamorphic minerals. (a and b) False color infrared and accompanying mineral map of an outcrop of serpentinite (gray in e and f) with dolomite (purple) and zones of enhanced serpentine signature (green) veins. The gravel around the outcrop (green) displays a stronger serpentine signal than the outcrop itself (unclassified; gray spectrum in panel e). Chlorite (aquamarine) is present in a fracture plane and some veins, while epidote (yellow) appears to be in the rock matrix, between several large veins of different compositions. Pyroxene (red) is present in clasts and in small amounts in the matrix of the serpentinite, as remnants of the protolith. Prehnite (orange) is also present in small clasts (white arrows, d). (e and f) Spectra corresponding to colored regions in b, d. Gray line at 0.97 µm shows the detector join, while atmospheric bands are transparent in field data. Detail from the key 2.1–2.45 µm region is shown in (h).

Serpentine-related absorptions are present throughout the outcrop with the strongest associated with veins. Serpentine absorptions of intermediate strength are found in the clasts surrounding the outcrop. Whitish veins in Figure 5a are mostly dolomite (purple in Figure 5b) but sometimes also contain serpentine or are surrounded by strong serpentine signals, stronger than the outcrop (green in Figures 5b and 5d).

We also see a number of minerals present over small spatial extents at this site, including clinopyroxene, chlorite, epidote, and prehnite (see Table 1 for mineral formulae). Clinopyroxene is identified by its absorption at ~1.03 μm and broad 2 μm absorption and is present in small areas within the outcrop and in several clasts, sometimes partially altered. As at the Al Qaryatayn site (Figure 3), being able to locate and sample or measure small amounts of unaltered rock is a useful capability to understand the history of alteration and probe protolith formation conditions with igneous minerals. In Figures 5b and 5d, we see chlorite in veins and along fracture planes, identified by the presence of a 2.25 μm Al/Fe^{3+} (or Mg)-OH combination band, in addition to a stronger Fe^{2+}-OH combination band at 2.35 μm (Bishop et al., 2008; Clark, 1999); a 1.39 μm OH band is hidden by atmospheric water. Epidote is also concentrated in specific areas but not confined to veins or fracture planes; it is at a nexus of intense serpentine, dolomite, and chlorite veins, and so may reflect enhanced alteration in that location. Epidote is spectrally similar to chlorite, with a minor absorption at 2.25 μm and deeper absorption at ~2.34 μm, but has an additional diagnostic feature at 1.56 μm (Clark, 1999; White et al., 2017). Prehnite is in clasts at millimeter-scale (Figure 5d); where in the rock, it closely follows banded plagioclase/pyroxene layers identified in field observations with hand lens, indicating that the alteration was localized. The banded pyroxene/plagioclase layers are not continuous, but are exposed in discontinuous patches in the outcrop. Prehnite is identified by its sharp 1.48 μm absorption, paired small absorptions at 2.23 and 2.29 μm, and larger 2.34 μm absorption.

Chlorite, epidote, and prehnite detected here are all minerals indicative of low-grade metamorphism (prehnite-pumpellyite facies), associated with moderate temperatures ~250–400°C and pressures 2–8 kbar (Frey & Robinson, 2009; Liou et al., 1983). Prehnite in particular is only stable within that temperature range and therefore is a useful indicator mineral for constraining the upper and lower bounds on the past temperature history (Liou et al., 1983). These minerals provide information on the composition of the protolith; chlorite, prehnite, and epidote are all aluminum-bearing and indicate that portions of the outcrop were not initially an ultramafic rock but likely were more mafic (and therefore aluminous) in composition. This is consistent with the geological context of the Wadi Dima site, located on a fault contact between mantle peridotite and layered mafic-ultramafic cumulates from the crustal section.

3.3. Listvenite (23.369 N, 58.185 E)

3.3.1. Listvenite Field Site

The listvenite field site is an exposed, erosionally smoothed outcrop within a dry wash (Figure 6), immediately downstream from (but stratigraphically above) the higher-grade metamorphic sole of the ophiolite. Listvenite is the end result of carbonation of a peridotite, where all Mg resides in carbonate minerals (magnesite ± dolomite) and Si is in quartz, usually with green chromian mica (muscovite-fuchsite solid solution and/or relict Cr-rich spinel; Halls & Zhao, 1995). Listvenite at and near this locality has been the subject of many studies (de Obeso et al., 2020; Falk & Kelemen, 2015; Nasir et al., 2007; Stanger, 1985; Wilde et al., 2002), and was sampled in rock core from Oman Drilling Project (OmanDP) Hole BT1B (Beinlich et al., 2020; Kelemen, Matter. et al., 2020; Menzel et al., 2020).

The image in Figure 6 was taken at a distance of ~2m. At this site, at small scale, we see predominantly magnesite throughout the rock matrix. The color map highlights zones of strongest magnesite, veins of dolomite, and other veins of magnesite with a very strong ~1-μm absorption (Figures 6c and 6d). Despite the wide, deep 1-μm absorption, common in minerals with ferrous iron such as olivine and siderite, the 2.3- and 2.5-μm carbonate absorption positions are consistent with magnesite rather than siderite (Figures 6g and 6h).

We also identify locally (Figures 6e and 6f) discrete clasts of distinctive non-listvenite lithologies, collected in local lows. Kaolinite, chlorite, and illite or muscovite are detected in pebbles of alluvium, collected in rock fractures. Kaolinite is identified by its characteristic asymmetric 2.17–2.21 μm absorption (Al-Al-OH combination band; Bishop et al., 2008), while muscovite has similarly sized absorptions at 2.22 and 2.35 μm.

3.3.2. Listvenite Hand Sample

A cobble from this site (Figure 7) shows the textures of magnesite with intergrown, light-green muscovite, and an opaque phase. While muscovites are available in spectral libraries, Cr-bearing fuchsite is not.

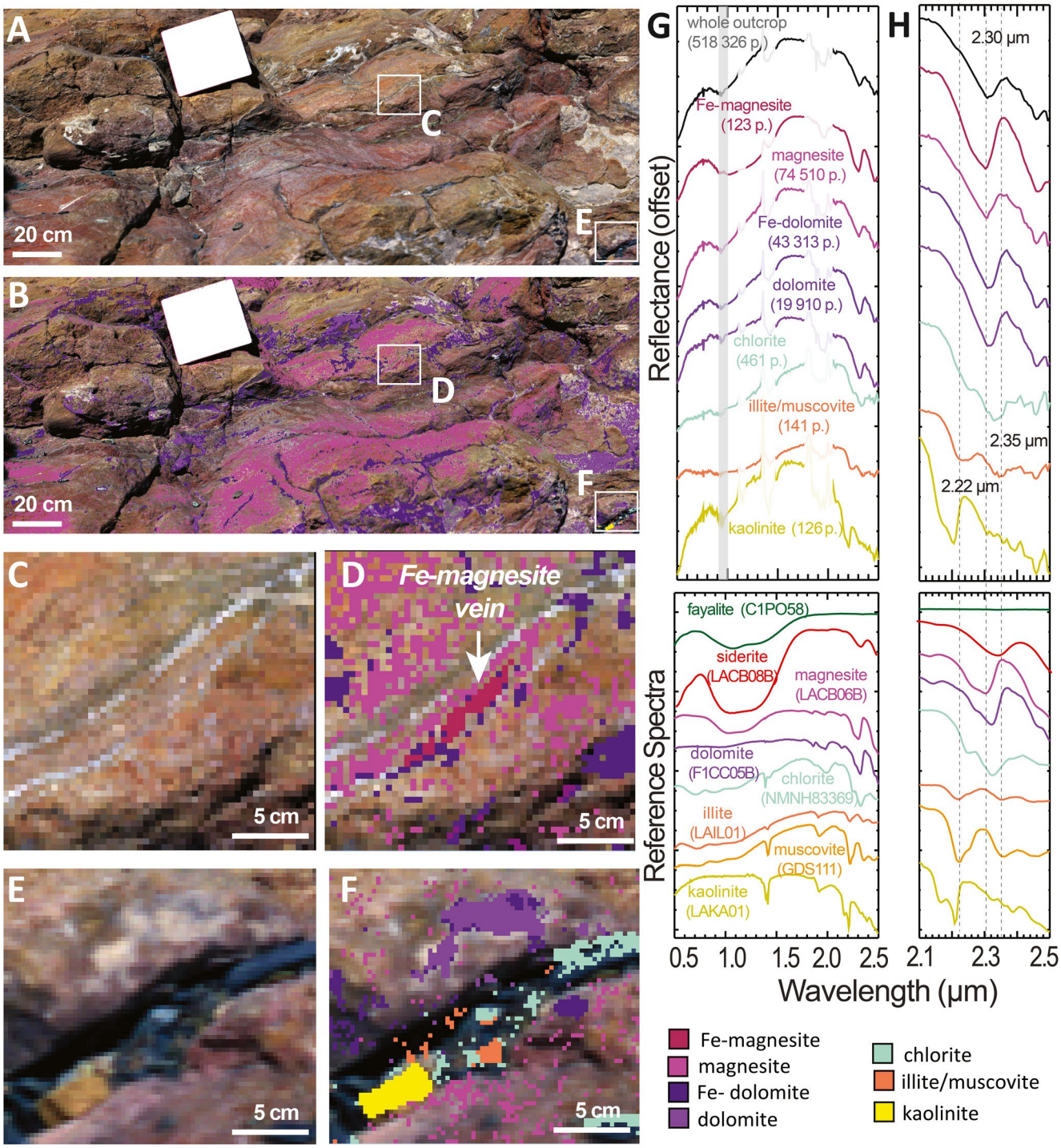

Figure 6. (a) Listvenite field site, located within a dry wash. Outcrop is veined, reddish, and smooth; whitish parts are later caliche-type cement. White square is a Spectralon panel, 30 × 30 cm. (b) Most of this outcrop appears to be magnesite (strongest signatures indicated in magenta) with veins of magnesite with a large 1 μm absorption (likely dues to trace amounts of ferrous iron; dark magenta; see panels c, d for detail), and some dolomite veins (dark purple), which have a minor 1 μm feature. Caliche deposits (light purple) are also dolomite and lack any trace of the 1 μm absorption. (c and d) Close-up of a vein of magnesite with a 1-μm absorption feature. The vein is between 2 white parallel veins, likely quartz (which is spectrally neutral in this range). (e and f) Close-up of clasts in bottom right of image. Clasts are identified by their absorptions between 2.1 and 2.5 μm; they are kaolinite (yellow), illite or muscovite (coral), and chlorite (aquamarine). (g) Mean spectra of each mineral mapped in in the outcrop and library spectra for reference. The gray bar is a spectral region with frequent artifacts due to the short and long wavelength detector joins, and semi-transparent regions are wavelengths of low signal due to absorption by atmospheric water vapor. (h) Close-up of the 2.1–2.5 μm region for spectra from (g).

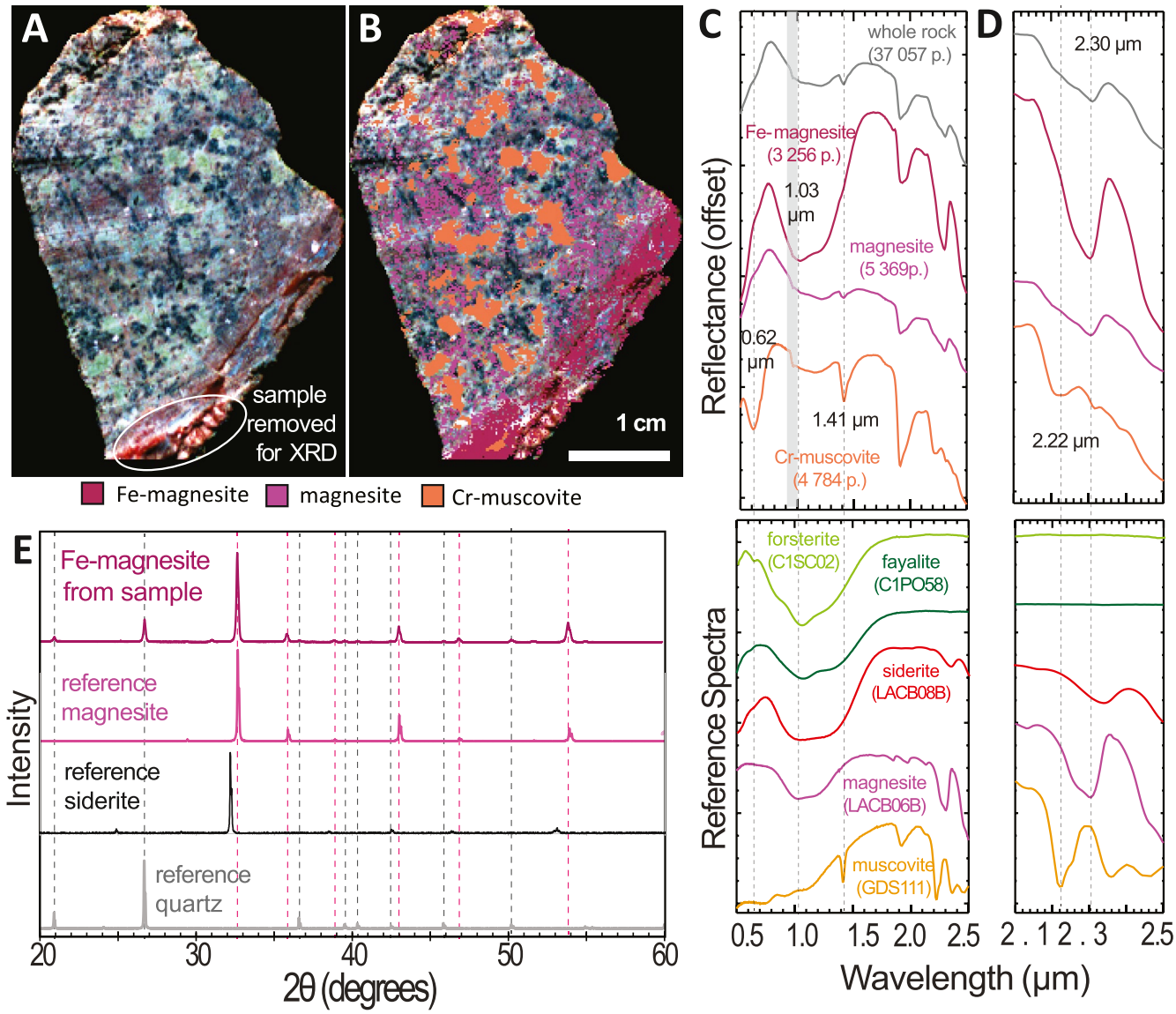

Figure 7. . (a and, b) Listvenite hand sample. Matrix is mixture of magnesite (magenta), Cr-muscovite/fuchsite (light green in visible; coral in parameter stretch), and opaques (like Cr or Fe oxides). (c and, d) Mean spectra of each mapped mineral over the full wavelength range (c) and a closeup on the 2.1–2.5 µm range (d). . In (c), the gray bar is a spectral region with frequent artifacts due to the short and long wavelength detector joins, and semi-transparent regions are wavelengths of low signal due to absorption by atmospheric water vapor. We were unable to find reference spectra for Cr-muscovite/fuchsite, which has a distinctive 0.62 µm absorption, likely causing its characteristic light green color. A vein on the bottom right of the sample has the strong 1-µm magnesite feature seen in field data (Figure 6), similar in shape and position to olivine (forsterite, fayalite). Our magnesite sample has wider 1-µm feature than the reference spectrum, indicating that the shoulders of this feature are not diagnostic. The lowest point of this asymmetric feature (~1.03 µm) lines up well with the lowest point of the forsterite absorption. (e) Diffraction peaks from XRD sample of Fe-magnesite vein show that it is a mixture of magnesite and quartz, with no olivine or siderite to cause the 1 µm absorption feature.

We therefore identify fuchsite based on a distinctive 0.62-µm absorption, which contributes to its green color and the 1.41- and 2.22-µm absorptions expected of muscovites with a small 2.35-µm absorption. Particularly given previous work in the area, we interpret the light-green muscovite as chromian mica (muscovite-fuchsite solid solution), while the opaques are probably relict Cr-spinel and/or Fe-oxides (Falk & Kelemen, 2015).

At the hand sample scale, we continue to observe select, distinctive veins of magnesite with a very strong, wide 1 µm absorption, which has a spectral appearance in terms of width and shape similar to that observed for olivine (e.g., Sunshine & Pieters, 1998). To determine whether relict olivine in this altered ultramafic

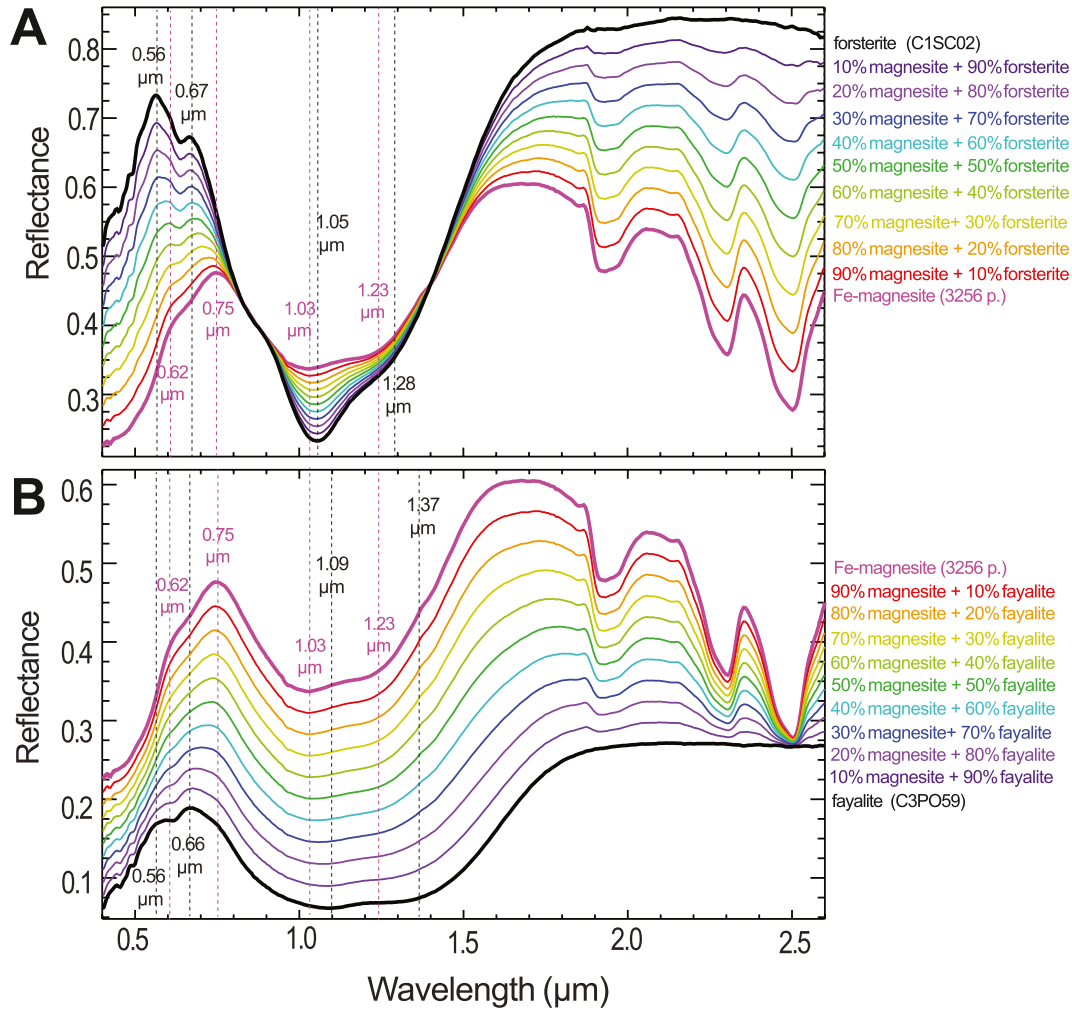

Figure 8. Computed linear spectral mixing of Fe-rich magnesite from the Oman imaging spectroscopy data set and olivines. (a) Mixing with forsterite. The reference forsterite sample (RELAB) is has a higher overall reflectance than the Fe-bearing magnesite (spectrum from our listvenite sample, Figures 9a and 9b). Here, the overall shape of the 1-μm absorption is very similar, with band centers offset by ~0.02–0.05 μm. In the VNIR, both forsterite and Fe-magnesite have 2 "peaks" from 0.5 to 0.7 μm between electronic absorptions. In forsterite, these peaks are shifted to shorter wavelengths (although minor Fe^{3+} weathering would alter the shape of this region). (b) Mixing with fayalite. The reference fayalite sample (RELAB) is has a lower overall reflectance than the Fe-bearing magnesite. Here, the overall shape of the 1-μm absorption is noticeably wider in fayalite than in magnesite, with band centers offset by ~0.06–0.14 μm. In the VNIR, fayalite peaks are at very similar positions as forsterite, though the relative heights are reversed.

rock could be partially responsible for the large 1-μm absorption (for characterization of olivine-nontronite-carbonate mixtures, see Bishop et al., 2013), we removed a small piece of this sample and crushed it for XRD analysis (Figure 7a). In Figure 7e, we see that the XRD peaks present in the sample correspond with magnesite and quartz (RRUFF IDs R040114 and R040031) with no olivine component. (Quartz has no absorption features in this wavelength region, so we would not expect to see its spectral signature). Thus, our XRD data are consistent with the documented, complete absence of olivine and the presence of Fe-rich cores in zoned magnesite crystals in listvenites near this site sampled by the Oman Drilling Project (Beinlich et al., 2020; Kelemen, Matter, et al., 2020).

We computed linear mixtures of Fe-bearing magnesite spectra with forsterite and fayalite endmembers to investigate in detail how the spectral properties of the 1-μm feature in olivine compares with our Oman Fe magnesite sample (Figure 8). Band centers in the 1-μm feature of Fe-magnesite are present at 1.03 and 1.23 μm, compared to 1.05 (1.09) μm and 1.28 (1.37) μm for forsterite and fayalite respectively. The 0.9-μm

absorption of the olivine triplet (e.g., Sunshine & Pieters, 1998) is not readily apparent, except as an absorption shoulder in forsterite. Between the shortest wavelengths and 1 μm absorption, local continuum maxima occur at 0.56 and 0.66–0.67 μm in olivine but at 0.62 and 0.75 μm in the Fe magnesite. These similarities are not unexpected because the wide 1-μm feature is due to absorptions from ferrous iron in an octahedral coordination environment in both mineral groups. Extensive studies of the 1-μm band have been conducted in olivines (e.g., Burns, 1993, and references therein) where the overlapping absorptions around 1-μm are attributed to ferrous iron in the distorted octahedral M1 and M2 sites. The 1-μm absorption in carbonate changes with grain size and iron content, and has been noted in the carbonate spectroscopy literature (e.g., Gaffey, 1985) but not systematically studied. Gaffey (1986) noted that even small amounts of iron in carbonates (0.5–3.5 wt% FeO) may cause large 1-μm features in carbonates, likely the effect being observed here with our Fe magnesites. The subtle distinguishable differences between carbonate-olivine mixtures and Fe magnesites that are discerned in two-component mixtures measured in lab may be too subtle for unique discrimination in remote sensing data (see discussion, in Section 4.3.1).

3.4. Travertine (22.815 N, 57.838 E)

At the travertine site, modern carbonate deposits have precipitated from hyperalkaline springs on top of dark, veined, partially to completely serpentinized peridotite (Figures 9–12). The travertine deposit is about 1 m high, imaged from a distance of ~3.5 m. Mountains in the background are >500 m away. These figures are part of the same image, with the right side (Figures 9 and 10) highlighting mineral signatures, and the left side (Figure 12) showing the range of biology-related spectral features. The sedimentological and mineralogical properties of this site were detailed in Leleu et al. (2016).

3.4.1. Calcite Natural Variability

White-gray-tan-brown rocks are emplaced on top of a dark gray unit in the bottom right, with dark mountains in the background (Figure 9a). Spectra of the white-gray-tan-brown rocks in the foreground are consistent with calcite, with homogenous carbonate absorption position regardless of the visible color. The distant mountains have a vein of carbonate (Figures 9c and 9d) where the absorption positions are consistent with dolomite (2.32 μm) rather than calcite (2.34 μm). The dark unit underlying the carbonate and composing the mountains has spectral properties consistent with Mg serpentine.

Calcite exhibits a variety of colors—light reddish brown colors are most common while white to dark gray colors correspond with a now-dry water spillway (Figures 10a and 10b). In VNIR data (Figures 10c and 10d), the spectral slope varies from flat to steep. In addition to variation in the color of the carbonate due the small compositional and grain size variation, select pixels have broad VNIR absorptions between 0.5 and 0.9 μm that likely indicate iron oxides, such as hematite, goethite or ferrihydrites. In the SWIR spectra (Figures 10d and 10e), all the carbonates have the diagnostic 2.34 and 2.5 μm absorptions of calcite but with considerably varying depths. Pixels that are not classified with our chosen band depth parameter thresholds (e.g., some of the whitish material in the travertine) have shallow absorptions, which is consistent with fine-grained calcite. These white-gray colored calcites occur closest to water, and they may be most recently formed by crystallization. Reddish calcites have deep absorption features consistent with coarse crystals; in one case, we see a minor 2.15 μm absorption in field data typically only seen in pure reference samples in laboratory (e.g., Gaffey, 1986).

3.4.2. Calcite and Serpentine Detectability

Both the average spectrum of the whole outcrop viewed on the ground and the airborne spectrum over ~500 m^2 from HyMap looking down on the outcrop (Figures 9e and 9f) are consistent with calcite with a strong absorption at 2.34 μm, downturn to 2.5 μm, and no 2.12-μm serpentine absorption. The spectral dominance of carbonate at larger spatial scales may be partly due to the high albedo contrast and partly due to geometry. In the side-looking field image, 18% (297,960/1,699049) of pixels are classified as serpentine and >48% (807,020/1,699049) of the pixels are calcite. The remaining pixels have weaker absorptions consistent with these that did not meet the strict criteria. The partially to completely serpentinized peridotites are very dark, and so while diagnostic absorptions may be relatively deep, the absolute depth is much smaller than similarly deep absorptions in bright materials. Viewing geometry (Pinet et al., 2017) likely also plays a role,

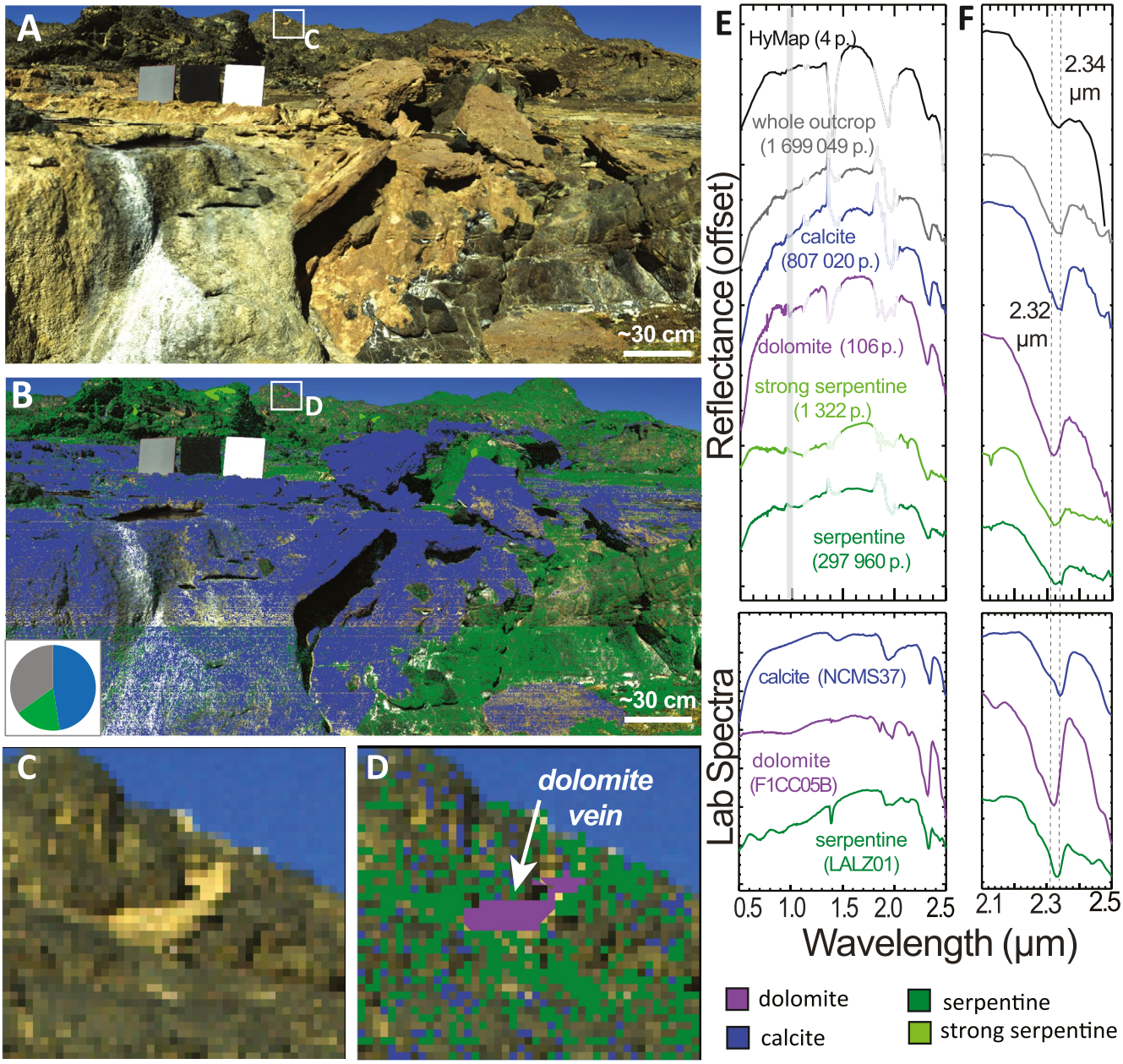

Figure 9. Travertine field site. (a) Approximate true color image; spectralon panels are 30 × 30 cm. (b) Mineral mapping utilizing parameters shows that most carbonate is calcite (blue) while the dark rocks in the foreground and background are serpentine (green). Overall, ~48% of the pixels in this image are classified as calcite, while ~18% are serpentine; mixed pixels not classified as either serpentine or carbonate make up the remaining 34% (gray in pie chart) and there is <1% dolomite. Their combined spectrum (gray in e and f) is most consistent with calcite. (c and, d) A vein in the mountains in the background shows a carbonate with a clear 2.32 µm absorption, consistent with dolomite (purple), in contrast to the 2.34 µm calcite absorptions in the travertine. e and f) Spectra corresponding to colored regions in b and d. Gray line at 0.97 µm shows the detector join, while atmospheric bands are transparent in field data. Detail from the key 2.1–2.45 µm region is shown in (h).

as in nadir-looking data such as Hymap observations, the overlying travertines might occupy more of the overall area.

Linear mixing results between an average calcite (Figure 11a) or coarsely crystalline calcite (Figure 11b) endmember and a serpentine endmember from the site show the challenge of serpentine detection in the dominantly areal % calcite scene. Using the average endmembers, the diagnostic 2.12 µm serpentine absorption flattens out at ~50% calcite/serpentine (becoming convex at ~70% calcite). The absorption center

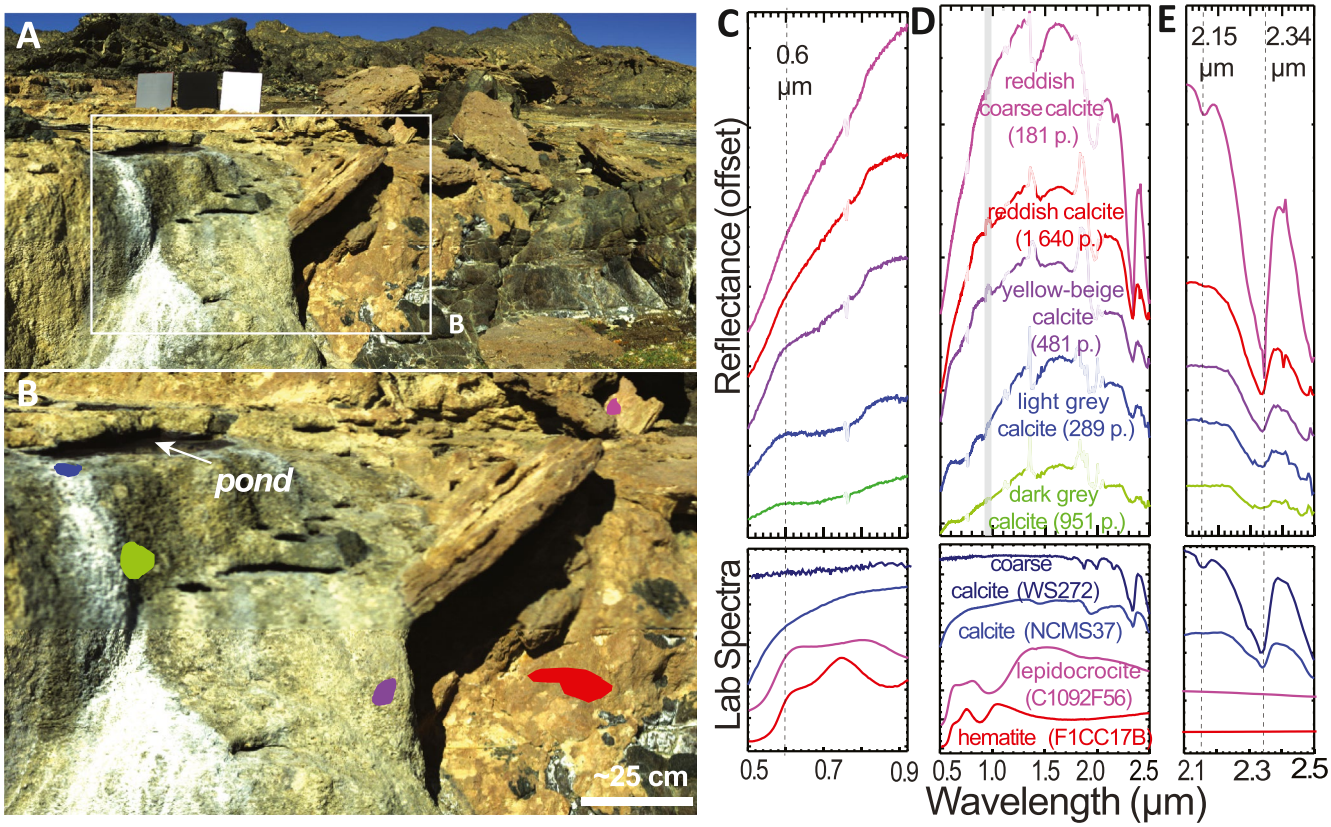

Figure 10. Travertine field site in Figure 9a with a zoom (b) to highlight diversity amongst calcite spectra in the same scene. (b) Average spectra of each colored region that are shown in (c and–e). Older calcite appears reddish while light and dark gray calcites are closer to the waters and in water appears to be a recent spillway. (c) In VNIR wavelengths, these calcite spectra have a wide range of slopes, and some (especially yellow-beige calcite (purple), and light gray calcite [blue]) have features at ~ 0.6 μm that may be related to iron oxides (e.g., hematite) and hydroxides (e.g., goethite). (d) Full spectral range (0.5–2.5 μm) of these different natural calcite examples, showing the differing overall shapes. (e) All spectra have the 2.34 μm absorption and 2.5 μm slope of calcite, although the band center is broader and shallower in the dark and light gray calcite spectra (green and blue) that may be most recently precipitated. Redder, older calcites have deeper band depths; in some cases, calcite absorptions at 2.15 μm are visible. In spectral plots, the gray bar is a spectral region with frequent artifacts due to the short and long wavelength detector joins, and semi-transparent regions are wavelengths of low signal due to absorption by atmospheric water vapor.

shifts from 2.32 μm (serpentine) to 2.34 μm (calcite) by ~40–50% calcite. The mean spectrum for the whole outcrop (gray; Figure 9e) has a flat (but not convex) 2.1 μm region and a band shifted to 2.34 μm, as expected for ~50% calcite. With instead the bright, coarsely crystalline calcite endmember (Figure 11b), the 2.1-μm region takes on the characteristics of crystalline carbonate, a narrow absorption at 2.15 μm, by ~40% calcite. The 2.3-μm band center shifts to calcite wavelengths away from serpentine with just ~20% calcite in the linear mixture.

3.4.3. Biological Materials

Vascular plants are the most common biological materials in our scene and have broad, deep water-related absorptions at 1.2, 1.4, and 1.9 μm, and dry vegetation also shows absorptions at ~1.7 and 2.1 μm, related to lignins, proteins, and cellulose (Kokaly et al., 2007; Peterson & Hubbard, 1992; Figure 12f). Dry vegetation (Figure 12e) has featureless red slopes similar to some of the calcites in Figure 11c. Green leaves on a bush show a chlorophyll-a absorption at 0.68 μm (e.g., Hubas et al., 2011), which is muted in the brownish vegetation in the near-field and far-field.

The cloudy stream, which is forming calcite terraces in the foreground, has distinctive spectral signatures of biological materials. Within the stream and in the wetted margins a weak 0.624-μm absorption, consistent with phycocyanin, a pigment in cyanobacteria, and a deeper 0.869-μm absorptions, consistent with bacteriochlorophyll–a, are consistently found with varying absorption strengths. These absorptions are not present in vascular plants (Hubas et al., 2011). Instead, these absorptions are consistent with microbial mats

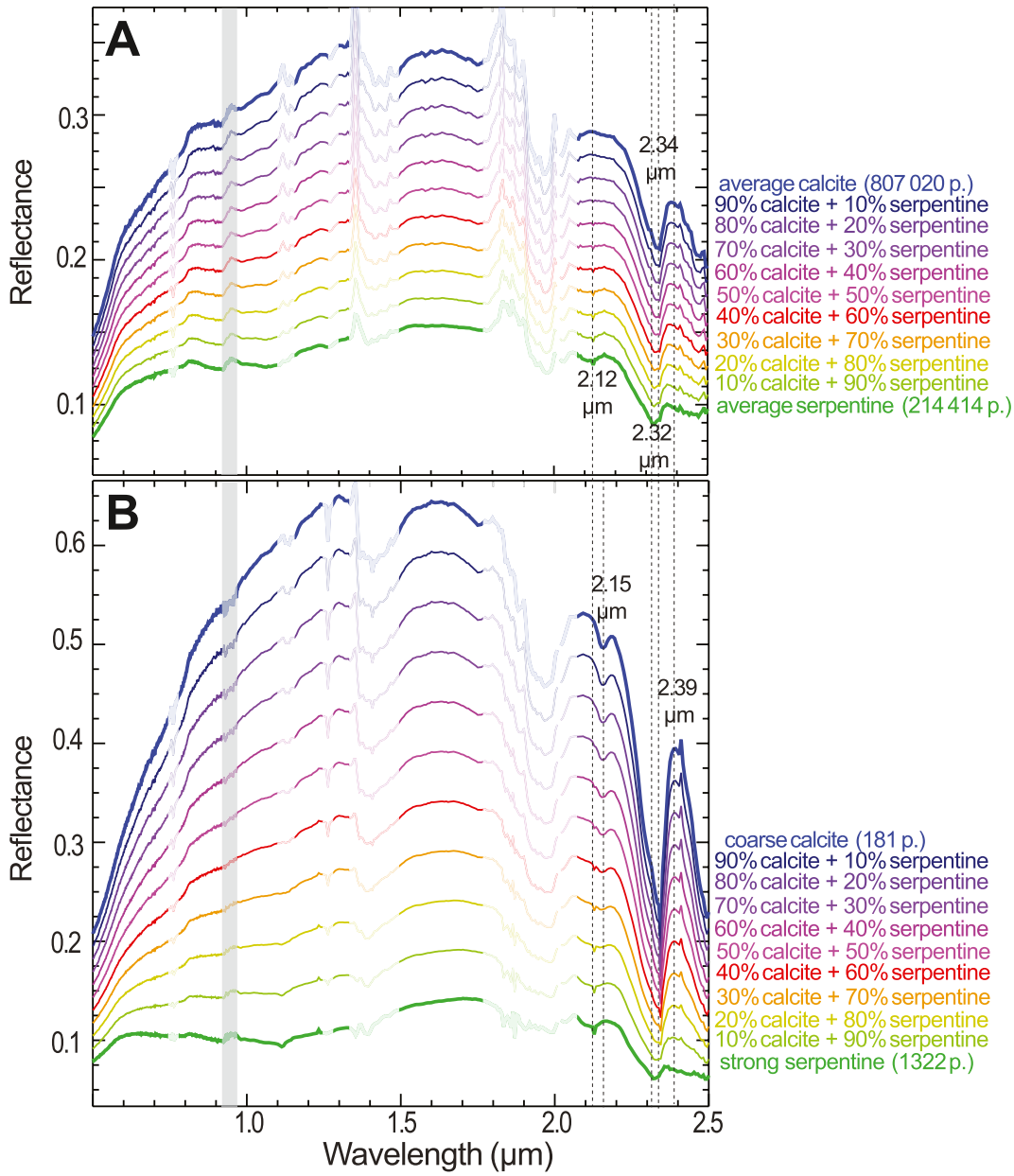

Figure 11. Computed linear mixtures between serpentine and calcite (spectra from travertine field site, Figure 9). (a) Average calcite and serpentine endmembers. The diagnostic Mg serpentine absorption at 2.12 μm flattens out at about 50% calcite/50% serpentine, and becomes convex at ~70% calcite. By 40%–50% calcite, the serpentine band center at 2.32 μm has shifted to 2.34 μm, and the 2.4 μm "peak" is broader and more similar to calcite. (b) Using a coarsely crystalline carbonate endmember (with deep absorptions) from within the scene, we see that the 2.1 μm region takes on a crystalline carbonate-like character (narrow, centered at 2.15 μm) by ~40% calcite/60% serpentine. Here, the 2.3-μm band center and 2.4 μm "peak" shape have shifted to calcite wavelengths by ~20% calcite/80% serpentine. In spectral plots, the gray bar is a spectral region with frequent artifacts due to the short and long wavelength detector joins, and semi-transparent regions are wavelengths of low signal due to absorption by atmospheric water vapor.

(e.g., Kokaly et al., 2007). In the mid-distance, where we first see the stream appear, the absorptions are particularly strong. This zone may be more densely colonized by microbial mats because of a food/energy source, for example upwelling methane/hydrogen from serpentinization. Notably, the microbial mats are quite spectrally distinct from chlorophyll-containing biological materials. Were we to design a field campaign testing the biological or biochemical diversity, we could use imaging spectroscopy to find hotspots of particular interest and perhaps even map microbial mat communities within the springs.

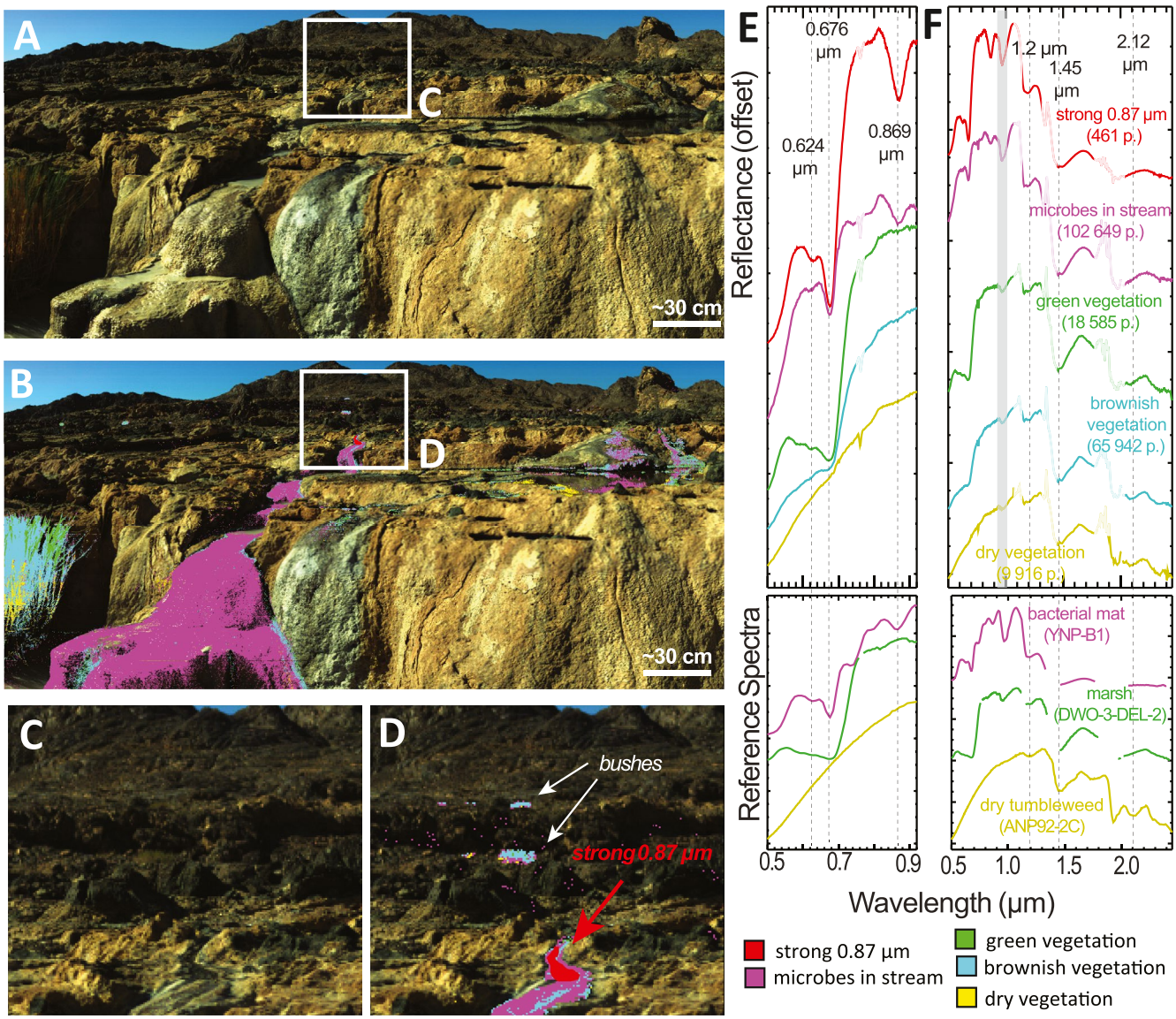

Figure 12. (a) Travertine field site with active travertine terraces and water flow. (b) Different colors map different biological materials with corresponding spectra in panels E, f. In the streams, magenta and red have absorptions at 0.624 and 0.869 µm consistent phycocyanin and bacteriochlorophyll-a, respectively, in microbial mats. Fresh, green vegetation (green) has a chlorophyll-a absorption at 0.676 µm, with a "green peak" around 0.550 µm. Brownish vegetation (cyan) lacks the green color peak, but still has the "red edge" between 0.68 and 0.75 µm. Dry vegetation (yellow) lacks diagnostic features in the VNIR, but shares the 1.2 µm absorption with all organic material, as well as the 1.45 and 2.12 µm absorptions related to lignin and cellulose which emerge when the deep, wide absorptions at 1.4 and 1.9 µm caused by water are reduced during drying out. (c and d) In the midground of the image are some individual bushes, as well as a very strong microbial absorption signal. The relative strength of these absorptions at this location indicates denser colonization, suggesting that this may a localized energy or nutrient source or other favorable environmental condition. In (e and f), the gray bar is a spectral region with frequent artifacts due to the short and long wavelength detector joins, and semi-transparent regions are wavelengths of low signal due to absorption by atmospheric water vapor.

4. Discussion

4.1. Advantages of Imaging Spectroscopy Versus Point Sampling

Our survey shows that imaging spectroscopy in the field has several advantages over discrete sampling. First, we readily distinguish between phases occurring in proximity that are visually very similar (e.g., dolomite and calcite), and thereby capture more of the full mineralogical diversity in an outcrop than would otherwise be obtained with sparser sampling. Furthermore, in situ imaging spectroscopy aids interpretation of the mineral phases in their original context with clear mapping of cross-cutting features to their

composition and compositional variability to better understand their temporal relationships. Field based imaging spectroscopy data also demonstrates the ability to pinpoint uncommon phases and map their spatial associations for further targeting/sampling. These uncommon phases provide additional information about the geologic history of the physical/chemical environment (e.g., prehnite and epidote in Figure 5). Some rare phases such as relict olivine and ortho- and clino-pyroxenes indicate the nature of the protolith. In extraterrestrial samples, finding small, less altered parts of an outcrop to measure/sample in situ could help us understand both the original igneous, metamorphic or sedimentary processes that created the rock (e.g., mantle conditions) as well as fluid processes and later changes in temperature and pressure that have shaped the alteration mineral assemblage.

Analysis of VSWIR imaging spectroscopy data readily detect atypical clasts amongst the cobbles at Wadi Dima and the listvenite site, allowing targeted sampling of the upstream lithologic diversity, including that of geologic units far from the site. The listvenite site illustrates the power of imaging spectroscopy to gain information, even about geologic units not at the locale. At this site, the more aluminous clasts have been transported downstream from below the basal thrust of the ophiolite, where aluminous metasediments are present in the metamorphic sole and common in the regionally extensive Hawasina Formation underlying the ophiolite. They allow us to explore the mineral diversity of the watershed without having to access it directly—analogous to rock clasts in sandstones, conglomerates or impact breccias that may be present in and around Jezero crater, the landing site for Mars 2020.

4.2. Detecting and Mapping Biological Materials

VSWIR imaging spectroscopy was highly effective in detecting and discriminating biological materials in the field by measuring pigments in the VNIR and detecting structural C-H and C-N in the SWIR in wavelengths at 1.7 and 2.1 μm. In particular, the unique pigments in microbial mats could be distinguished from chlorophyll, allowing ready discrimination in images (Figure 12). Additionally, within the stream course, locales relatively more colonized by bacterial mats were easily identified, pointing to a means to spatially map communities and ascertain the environmental gradients–in this case, we hypothesize an additional water or gas seep–driving heterogeneity. Thus, in addition to geological applications, ecological studies involving spatial mapping of species are possible and future work might explore the small scale distribution of different microbial mat communities as a function of water chemical gradients. Relevant to planetary exploration, microbialites associated with rocks were straightforwardly mapped relative to mineral deposits.

4.3. Lessons for Carbonate and Serpentine Detection on Mars

4.3.1. Mineral Identification

At meso-scale and smaller spatial scales in the data from Oman, we use the shortwave-infrared imaging spectroscopy data to confidently identify and map many important minerals and distinguish between minerals that are indistinguishable in color imagery. One example is the ready distinction between calcite, dolomite, and magnesite, where multiple phases are present as whitish carbonate veins within a scene. Indeed, shortwave infrared imaging spectroscopy of outcrops in the Samail ophiolite, Oman, allows reconstruction of changing conditions, tracing *in situ* magnesite formation, serpentine formation, and calcite formation from precipitation from discharging waters that have participated in serpentinization. Observed carbonate compositional variability and cross-cutting relationships record well the classic geochemical and hydrological processes first described in Barnes & O'Neil (1969). In uplifted serpentinized ocean crust, surface waters and ground waters further weather the outcrop to form Mg-Ca carbonates from olivine and pyroxene; serpentinization occurs at depth, and outflowing alkaline groundwaters from the serpentinization process form Ca-rich carbonate travertine deposits.

Except for when associated with altered ultramafic rocks, magnesite is rarely the dominant carbonate mineral on Earth. In Oman, dolomite, Mg,Ca-carbonate, is comparatively more spatially widespread. On Mars, where we detect carbonate in ~20 m/pixel orbital data (e.g., Ehlmann et al., 2008; Niles et al., 2013), the band centers are consistent with magnesite instead of the longer wavelengths of dolomite, calcite, and siderite. None of our study sites in Oman have HyMap airborne spectra consistent with magnesite alone (Figure 2), probably due to spatial mixing with serpentine. Of the sites in the Samail ophiolite that we visited

with an imaging spectrometer, only the listvenite site had a dominantly magnesite signature (averaged over the whole rock outcrop, tens of square meters; Figures 6g and 6h), identified by paired absorptions centered near 2.30 and 2.50 μm (Gaffey, 1985). This suggests that the phase observed from Mars orbit is magnesite, although the processes of its formation or the nature of the protolith are likely not precisely analogous to the magnesite-dominated listvenite environments we have encountered in Oman. The rocks on Mars are more Fe-rich; this and other aspects of protolith composition likely exert control over water chemistry and resultant metal cations in the carbonate phase.

Another finding relevant to interpretation of data from Mars are the Fe-bearing magnesites found at the listvenite site (Figures 7 and 8). The carbonate vibrational absorptions are at positions characteristic of magnesite, even though there are also strong, broad electronic absorptions due to ferrous iron in the octahedral site. This confirms in the field Gaffey (1986) laboratory data showing similar behavior for very low wt. % Fe in carbonates. There are subtle differences in position of the 1 μm absorptions that could distinguish olivine from Fe-containing carbonate in the laboratory, but for remote sensing data the short wavelength maximum at 0.75 μm for carbonate versus <0.67 μm for olivines is a clearer indicator because of the magnitude of the feature and its spectral shift. A complication, however, is that the presence of ferric oxides will also dictate the position of this features. Such a complication is particularly acute on Mars because of the near-ubiquitous Fe(III)-oxide bearing dust, which dominates VNIR spectral properties to a much greater extent than for the Fe(III)-oxide patinas on the outcrops in Oman. On Mars, magnesite spectra almost always occur with deep ~1 μm bands, interpreted to permit Fe in the carbonate but largely result from mixing of magnesite with regionally widespread olivine (e.g., Brown et al., 2020; Ehlmann et al., 2008). Here, the fact that olivine occurs without carbonate in other pixels lends credence to the interpretation. Nonetheless, spectral variation in infrared spectra from carbonate-bearing rocks on Mars, including the Nili Fossae region, should be re-examined with alternative hypothesis that the 1-μm feature could be Fe magnesite in mind, as suggested recently by (Horgan et al., 2020). Additional future high spatial resolution thermal imaging spectroscopy from orbit or visible/shortwave infrared spectroscopic and compositional data at smaller scales, such as provided by the Mars-2020 rover, should be able to distinguish between olivine-bearing mixtures with carbonate and Fe-magnesite samples.

4.3.2. Detecting and Estimate Abundance of Serpentine and Carbonate in Mixtures

Having data available at a number of spatial scales (e.g., Figure 3), particularly sub-cm-scales, is useful to isolate spectral endmembers to the greatest extent possible and develop approaches to compute quantitative abundances from mixing relationships. For this Oman work, the multi-scale nature of the data, from 10s m/pixel airborne data to 250 μm/pixel hand sample data, permit us to isolate the spectral properties of endmembers and then use the proportions of veins and properties of spectra at different scales to estimate the total amount of mineralization within veins in the rock unit, providing estimates of, for example, ~22 area% carbonate in Al Qaryatayn at both cm-scale and mm-scale.

Most planetary datasets are not multi-scale. Instead, non-linear radiative transfer modeling with known endmembers has been shown in laboratory experiments to yield accurate abundance estimates for some bulk mineral mixtures and applied to orbital data (Lapôtre et al., 2017; Mustard & Pieters, 1989). Our data indicate why quantitative unmixing is considerably more complex in airborne or orbital remote sensing, when we do not know the exact spectral endmembers. The accuracy is diminished for minerals with solid solution compositional variability and textural variability, that is, many geological materials. Endmembers from within a scene may themselves be mixtures down to sub-100 μm scale. Thresholds of detectability limited by the textural and crystallinity characteristics of the endmembers at scales not easily incorporated into existing radiative transfer modeling. Also, crucially, these Oman data show how the precise nature of the endmembers dictates detection thresholds, at least in serpentine-carbonate mixtures.

At the resolution of field data (cm's/pixel), we can generally distinguish between Mg serpentine and carbonates, despite their similar absorption features, because some pixels occur where they are relatively purely one or the other. This allows, first, detection of the existence of endmembers and, second, and ability to understand how the spectral signatures would mix at different scales. An examination of the behavior of some of the most diagnostic spectral characteristics of carbonate-serpentine mixtures (Figure 13) clearly shows strengthening of a 2.12 μm feature and increased asymmetry at 2.3 μm and at 2.5 μm as the quantity of serpentine versus carbonate increases in both natural rocks, natural rock powders, and synthetic

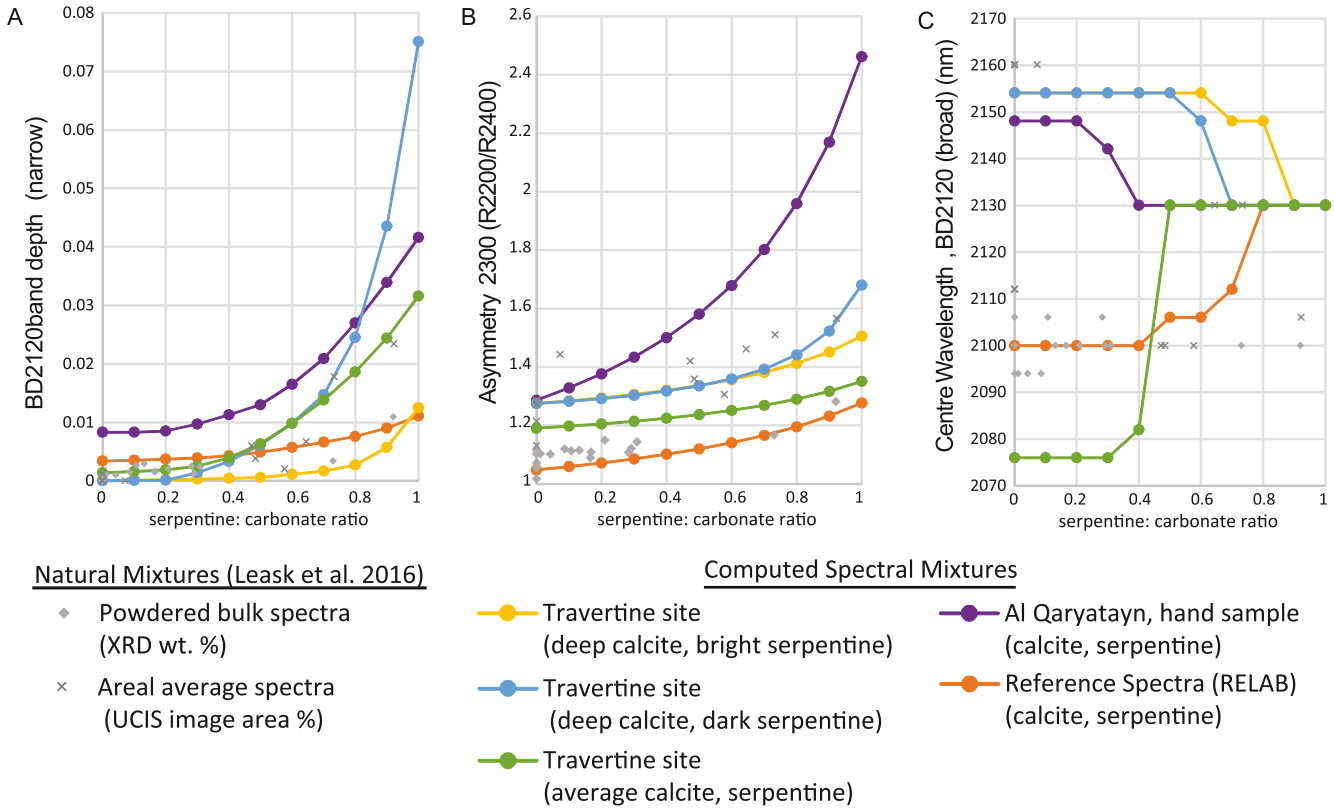

Figure 13. Spectral parameters for samples with mixtures of carbonate and serpentine. Gray x's and diamonds are from average spectra of Oman samples measured in Leask & Ehlmann (2016), subset to those samples with Mg serpentine and carbonate combined at >60 wt.%. Areal average spectra from microimaging spectroscopy data of these samples with the Ultra Compact Imaging Spectrometer (UCIS; Van Gorp et al., 2014), plotted as a function of serpentine:carbonate by % area. Bulk spectra of powders of subsets of the same samples are plotted by % weight XRD. Colored points and lines utilize computed endmember mixtures of pairs of calcite and serpentine from our Oman field sites in this work or the RELAB library. (a) The band depth of the 2.12 μm metal-OH absorption band characteristic of Mg serpentine, (b) the asymmetry of the 2.3 μm band becomes more pronounced in serpentine, (c) the center wavelength of the 2.1 μm band.

mixtures. However, the absolute values of these parameters are rarely uniquely diagnostic of composition because serpentine and carbonate mineral endmember spectra are heterogeneous due to textural and solid solution chemical variation. While the directionality of the parameters is the same in mixtures with different carbonate-serpentine endmember combinations, the variability in absolute values between different mixtures at the same proportionality is sometimes comparable to the range of parameter values for a 0%–100% mixture of two particular serpentine and carbonate endmembers (Figure 13). For example, based on the spectral data of our mixtures, serpentine present at >40–50 area% produces a band depth at 2.12 μm of greater that 1%, but the relationship between serpentine area% and band depth is not linear and varies by mixture. Conversely, no conclusion can be made about the absence of serpentine as lower than 1% band depths at 2.12 μm are observed in some carbonate-serpentine endmember mixtures, even with >50% serpentine (Figure 13a). Because band position shifts depend on both the content of serpentine and the cation of the carbonate mixed with the serpentine, they are similarly not reliable indicators, alone, of the presence of serpentine versus carbonate (Figure 13c).

Thresholds of detection for Mg serpentine and carbonate when mixed with the other are 20–30 area%, sometimes larger. Data from our field investigation highlight how Mg serpentine can "hide" carbonate and vice versa: a serpentinite outcrop at Al Qaryatayn with ~40 area% carbonate in fine, ~1–50 mm veins is spectrally indistinguishable from pure serpentine from a standoff distance of ~30 m, while at the travertine site an outcrop of >48 area% carbonate and 18 area% Mg serpentine looks like pure carbonate from aerial surveys. In Figure 11, well-crystallized calcite disguises the presence of serpentine at merely 20 area% calcite, whereas finely crystalline calcite does not have this effect until >40 area% calcite.

Difficulty in definitively identifying Mg serpentine within carbonate (or vice-versa) from shortwave infrared spectral data represents a real challenge in interpreting planetary surface observations. This is highlighted with regard to interpreting the origin and environmental significance of the "olivine-carbonate" unit that is present in and around Nili Fossae and at the Mars-2020 landing site of Jezero Crater. As a simple example, the presence of serpentine throughout would indicate that most of the alteration occurred at a high partial pressure of H_2O, whereas olivine can be altered to anhydrous mixtures of magnesite + quartz in CO_2-rich environments with low partial pressures of H_2O, similar to the present Martian atmosphere via $Mg_2SiO_4 + 2CO_2 = 2MgCO_3 + SiO_2$ (Kelemen, Evans, et al., 2020). Serpentine is only rarely detected here and elsewhere on Mars (Ehlmann & Mustard, 2012; Ehlmann et al., 2010; Amador et al., 2018). This may indeed indicate that serpentine is rare on Mars, or instead, our work in Oman shows that Mg serpentine could be present at abundances <~20 to 40 area% even while not being detected as a discrete phase. For the Nili Fossae "olivine-carbonate unit" this could either be due to the bulk lithology lacking serpentine or particular spatial relationships between the phases (e.g., carbonate mixtures with or coatings atop serpentine). At 18–40 m/pixel in CRISM data, Oman-like travertine calcite has been searched for and so far not found in the Nili Fossae region, though calcite spectral properties are similar enough to serpentine-magnesite mixtures to complicate detection at low abundance.

Examination of trends like those in Figures 4, 11, and 13 offers a means to identify the presence of multiple endmembers from orbital or landscape-scale data, if there is spatial heterogeneity in endmember abundance at the sampling scale to extrapolate mixing trends. Future in situ spectroscopy and compositional data can resolve some of these outstanding questions (e.g., Martin et al., 2020). For example, the Mars-2020 rover will carry a shortwave infrared point spectrometer for identification of outcrops with carbonates and/or serpentine from a distance at cm-to mm-scale. Visible/near-infrared data from multispectral cameras will provide contextual images. Subsequent in situ examination of these outcrops by Mars-2020s microscopic mapping x-ray fluorescence and deep-ultraviolet Raman spectrometers, which make measurements at 100-μm/spot scale, will establish approximate mineral proportions and allow detection of minor phases.

5. Conclusions

With a VSWIR imaging spectrometer in the field, spatially resolved compositional maps covering whole outcrops were effective in pairing textural changes to compositional changes to delineate lithologies, discern cross-cutting relationships between alteration phases, and detect many minor phases of importance to determining the geologic history. With compositional maps derived from scene spectra, we were able to distinguish visually similar compositions, distinguish different carbonate and hydrous silicate minerals to trace the evolution of fluid compositions, identify rare minerals such as small remnant pyroxenes within the matrix of the rock, identify minor metamorphic products like prehnite, and find clasts transported from more distant lithologies. Detection and identification of rare primary phases is important because it identifies cm-scale locales for targeted follow-up investigation to determine the original composition and geological processes that formed the protolith with the minimum amount of overprinting alteration. Rare minerals of metamorphic assemblages provide additional constraints on the temperature and pressure conditions, and so being able to detect less common phases constrains the possible ranges of past environmental conditions. In situ imaging spectroscopy can thus complement and augment traditional field geological approaches for analysis.

The ability to spatially characterize mineralogical variability at a site is particularly useful on planetary missions, where the number of samples and sites visited are limited, and it is essential to rapidly extract the most information possible from each sample and site. For this kind of mineralogical characterization, the utility of high spectral and spatial resolution VSWIR imaging spectroscopy has been demonstrated, and coverage of the 1.0–2.6 μm SWIR spectral range is crucial for mineral identificaiton. VNIR-only camera systems (spectral range <1 μm) cannot distinguish between similar materials (e.g., prehnite, epidote, chlorite, serpentine; dolomite vs. calcite vs. magnesite) and single point VSWIR spectrometers are more challenged in finding less common phases and characterizing their spatial relationships due to sparse sampling.

For mafic and ultramafic rocks almost completely altered by carbonation and serpentinization, this study also highlights the challenges of remote identification and quantification of mineral abundances in rocks

at coarse spatial scale due to spectral interferences, non-linear mixing effects, and endmember variability. Detection thresholds of either serpentine or carbonate in serpentine-carbonate mixtures are ~20 area% and sometimes higher. For terrestrial studies where access to a site for field-based imaging spectroscopy or access to hand samples from the site for lab-based imaging spectroscopy is possible, identifying the spectral properties of site-specific typical mineralogical endmembers can improve abundance estimates from remote imagery datasets. For planetary datasets, such endmember identification is rarely possible, and the challenges of the accuracy of abundance estimates warrants consideration. Additionally, while an orbit-based spectroscopic detection of a phase definitively indicates presence, this study highlights that one must take care when interpreting absence of a detection of a phase. The results of this work in Oman demonstrate that lack of orbital detection of serpentine in Mars carbonate-bearing units only constrains serpentine abundance to be <~50 area% relative to carbonate; it remains for future in situ investigation by the Mars-2020 rover to determine if serpentine is present in outcrops of carbonate near its landing site.

Data Availability Statement

Datasets used in this research are available in the CaltechDATA site (http://dx.doi.org/10.22002/D1.2028) and at the CaltechDATA site (https://doi.org/10.22002/D1.222) for data from our previous Leask and Ehlmann (2016) publication.

Acknowledgments
Thanks to the other members of our field party, Mathieu Rospabé, Mathieu Benoit, Said Al Musharrafi and Layla al-Habsi, and to the Bedouin family of Said Ghofar who hosted our field campsite in Wadi Dima. We appreciate also the help of Mohamed Al Araimi and of Mohamed Al Batashi from the Public Authority of Mining of Oman in reviewing and permitting our samples to bring to Caltech for further analyses. Thanks to Jesse Tarnas and Brad Garczynski who provided reviews that helped to improve this manuscript. We are appreciate the support of a NASA Mars Fundamental Research grant to B.L.E (#NNX12AB42G), a NASA Planetary Major Equipment grant to B.L.E. for the imaging spectrometer (#NNX13AG74G), and an NSERC PGS-D scholarship to E.K.L. R.N.G. thanks a grant from the American Philosophical Society's Lewis and Clark Fund for Exploration and Field Research in Astrobiology for supporting partial field and travel costs. P.P., Y.D., and G.C. were supported by the French Space Agency (CNES) in a project in conjunction with the Mars-Express mission OMEGA instrument.

References

Amador, E. S., Bandfield, J. L., & Thomas, N. H. (2018). A search for minerals associated with serpentinization across Mars using CRISM spectral data. *Icarus*, *311*, 113–134. https://doi.org/10.1016/j.icarus.2018.03.021

Amri, I., Benoit, M., & Ceuleneer, G. (1996). Tectonic setting for the genesis of oceanic plagiogranites: Evidence from a paleo-spreading structure in the Oman ophiolite. *Earth and Planetary Science Letters*, *139*(1–2), 177–194. https://doi.org/10.1016/0012-821x(95)00233-3

Barnes, I., O'Neil, J. R., & Trescases, J. J. (1978). Present day serpentinization in New Caledonia, Oman and Yugoslavia. *Geochimica et Cosmochimica Acta*, *42*(1), 144–145. https://doi.org/10.1016/0016-7037(78)90225-9

Beinlich, A., Plümper, O., Boter, E., Müller, I. A., Kourim, F., Ziegler, M., et al. (2020). Kelemen and the Oman Drilling Project Science Team, Ultramafic rock carbonation: Constraints from listvenite core BT1B, Oman drilling project. *Journal of Geophysical Research*, *125*, e2019JB019060. https://doi.org/10.1029/2019jb019060

Bibring, J.-P., Langevin, Y., Gendrin, A., Gondet, B., Poulet, F., Berthé, M., et al. (2005). Mars surface diversity as revealed by the OMEGA/Mars Express observations. *Science*, *307*(5715), 1576–1581. https://doi.org/10.1126/science.1108806

Bindi, L., Churakov, S. V., Downs, R., Gfeller, F., Krivovichev, S. V., Lafuente, B., et al. (2015). *Highlights in mineralogical crystallography*. Walter de Gruyter GmbH & Co KG.

Bishop, J., Lane, M. D., Dyar, M. D., & Brown, A. J. (2008). Reflectance and emission spectroscopy study of four groups of phyllosilicates: Smectites, kaolinite-serpentines, chlorites and micas. *Clay Minerals*, *43*(1), 35–54. https://doi.org/10.1180/claymin.2008.043.1.03

Bishop, J. L., Perry, K. A., Darby Dyar, M., Bristow, T. F., Blake, D. F., Brown, A. J., & Peel, S. E. (2013). Coordinated spectral and XRD analyses of magnesite-nontronite-forsterite mixtures and implications for carbonates on Mars. *Journal of Geophysical Research: Planets*, *118*(4), 635–650. https://doi.org/10.1002/jgre.20066

Blaney, D. L., Mouroulis, P., Ehlmann, B. L., Van Gorp, B., McKinley, I., Rodriguez, J., et al. (2016). Ultra compact imaging spectrometer. In: *3rd International Workshop on Instrumentation for Planetary Missions*. Abstract # 4067.

Boudier, F., Bouchez, J.-L., Nicolas, A., Cannat, M., Ceuleneer, G., Misseri, M., & Montigny, M. (1985). Kinematics of oceanic thrusting in the Oman ophiolite. Model of plate convergence. *Earth and Planetary Science Letters*, *75*, 215–222. https://doi.org/10.1016/0012-821x(85)90103-7

Boudier, F., & Coleman, R. G. (1981). Cross section through the peridotite in the Samail Ophiolite, southeastern Oman Mountains. *Journal of Geophysical Research*, *86*(B4), 2573–2592. https://doi.org/10.1029/jb086ib04p02573

Braun, M. G., & Kelemen, P. B. (2002). Dunite distribution in the Oman ophiolite: Implications for melt flux through porous dunite conduits. *Geochemistry, Geophysics, Geosystems*, *3*, 1–21. https://doi.org/10.1029/2001GC000289

Brown, A. J., Viviano, C. E., & Goudge, T. A. (2020). Olivine-Carbonate Mineralogy of the Jezero Crater Region. *Journal of Geophysical Research: Planets*, *125*, e2019JE006011. https://doi.org/10.1029/2019JE006011

Burns, R. G. (1993). *Mineralogical applications of crystal field theory*. Cambridge university press.

Canovas, P. A., III, Hoehler, T., & Shock, E. L. (2017). Geochemical bioenergetics during low-temperature serpentinization: An example from the Samail ophiolite, Sultanate of Oman. *Journal of Geophysical Research: Biogeosci.*, *122*, 1821–1847. https://doi.org/10.1002/2017JG003825

Carr, M. H. (1995). The Martian drainage system and the origin of valley networks and fretted channels. *Journal of Geophysical Research: Planets*, *100*(E4), 7479–7507. https://doi.org/10.1029/95je00260

Ceuleneer, G., & Nicolas, A. (1985). Structures in podiform chromite from the Maqsad district (Sumail ophiolite, Oman). *Mineralium Deposita*, *20*, 177–184. https://doi.org/10.1007/bf00204562

Chabrillat, S., Pinet, P. C., Ceuleneer, G., Johnson, P. E., & Mustard, J. F. (2000). Ronda peridotite massif: Methodology for its geological mapping and lithological discrimination from airborne hyperspectral data. *International Journal of Remote Sensing*, *21*(12), 2363–2388. https://doi.org/10.1080/01431160050030510

Chavagnac, V., Monnin, C., Ceuleneer, G., Boulart, C., & Hoareau, G. (2013). Characterization of hyperalkaline fluids produced by low-temperature serpentinization of mantle peridotites in the Oman and Ligurian ophiolites. *Geochemistry, Geophysics, Geosystems*, *14*, 2496–2522. https://doi.org/10.1002/ggge.20147

Chavez, P. S., Jr. (1988). An improved dark-object subtraction technique for atmospheric scattering correction of multispectral data. *Remote Sensing of Environment*, *24*(3), 459–479. https://doi.org/10.1016/0034-4257(88)90019-3
Clark, R. N. (1999). Spectroscopy of rocks and minerals, and principles of spectroscopy. *Manual of remote sensing*, *3*, 3–58.
Clénet, H., Ceuleneer, G., Pinet, P., Abily, B., Daydou, Y., Harris, E., et al. (2010). Thick sections of layered ultramafic cumulates in the Oman ophiolite revealed by an airborne hyperspectral survey: Petrogenesis and relationship to mantle diapirism. *Lithos*, *114*(3–4), 265–281. https://doi.org/10.1016/j.lithos.2009.09.002
Clenet, H., Pinet, P., Ceuleneer, G., Daydou, Y., Heuripeau, F., Rosemberg, C., et al. (2013). A systematic mapping procedure based on the Modified Gaussian Model to characterize magmatic units from olivine/pyroxenes mixtures: Application to the Syrtis Major volcanic shield on Mars. *Journal of Geophysical Research: Planets*, *118*(8), 1632–1655. https://doi.org/10.1002/jgre.20112
Cloutis, E. A., & Gaffey, M. J. (1991). Pyroxene spectroscopy revisited: Spectral-compositional correlations and relationship to geothermometry. *Journal of Geophysical Research*, *96*(E5), 22809–22826. https://doi.org/10.1029/91je02512
Cocks, T., Jenssen, R., Stewart, A., Wilson, I., & Shields, T. (1998). The HyMapTM airborne hyperspectral sensor: The system, calibration and performance. In: *Proceedings of the 1st EARSeL workshop on imaging Spectroscopy*. EARSeL.
Combe, J.-P., Launeau, P., Pinet, P. C., Despan, D., Harris, E., Ceuleneer, G., & Sotin, C. (2006). Mapping of an ophiolite complex by high-resolution visible-infrared spectrometry. *Geochemistry, Geophysics, Geosystems*, *7*, Q08001. https://doi.org/10.1029/2005GC001214
Cooley, T., Anderson, G.P., Felde, G. W., Hoke, M. L., Ratkowski, A. J., Chetwynd, J. H., et al. (2002). FLAASH, a MODTRAN4-based atmospheric correction algorithm, its application and validation. In: *IEEE International geoscience and remote sensing symposium*. IEEE.
de Obeso, J. C., & Kelemen, P. B. (2018). Fluid rock interactions in residual mantle peridotites overlain by shallow oceanic limestones: Insights from Wadi Fins, Sultanate of Oman. *Chemical Geology*, *498*, 139–149. https://doi.org/10.1016/j.chemgeo.2018.09.022
de Obeso, J. C., & Kelemen, P. B. (2020). Magnesium and iron mobility during serpentinization, oxidation and weathering of mantle peridotite at low temperatures: The case of Wadi Fins, Oman. *Philosophical Transactions of the Royal Society of London - A*, *378*, 20180433. https://doi.org/10.1098/rsta.2018.0433
de Obeso, J. C., Santiago Ramos, D. P., Higgins, J. A., & Kelemen, P. B. (2021). A Mg isotopic perspective on the mobility of magnesium during serpentinization and carbonation of the Oman ophiolite. *Journal of Geophysical Research: Solid Earth*, *126*, e2020JB020237. https://doi.org/10.1029/2020JB020237
De Sanctis, M., Ammannito, E., Raponi, A., Marchi, S., McCord, T. B., McSween, H. Y., et al. (2015). Ammoniated phyllosilicates with a likely outer Solar System origin on (1) Ceres. *Nature*, *528*(7581), 241–244. https://doi.org/10.1038/nature16172
Dewandel, B., Boudier, F., Kern, H., Warsi, W., & Mainprice, D. (2003). Seismic wave velocity and anisotropy of serpentinized peridotite in the Oman ophiolite. *Tectonophysics 370*, 77–94. https://doi.org/10.1016/s0040-1951(03)00178-1
Edwards, C. S., & Ehlmann, B. L. (2015). Carbon sequestration on Mars. *Geology*, *43*(10), 863–866. https://doi.org/10.1130/g36983.1
Ehlmann, B., Blaney, D. L., Green, R. O., & Mouroulis, R. (2016). VSWIR microimaging spectroscopy for geologic history and identifying and quantifying mineral, ice, and organic abundances on planetary surfaces. In: *3rd International Workshop on Instrumentation for Planetary Mission*.
Ehlmann, B., Mustard, J. F., & Murchie, S. L. (2010). Geologic setting of serpentine deposits on Mars. *Geophysical Research Letters*, *37*(6). https://doi.org/10.1029/2010GL042596
Ehlmann, B. L., & Mustard, J. F. (2012). An in-situ record of major environmental transitions on early Mars at Northeast Syrtis Major. *Geophysical Research Letters*, *39*, L11202. https://doi.org/10.1029/2012GL051594
Ehlmann, B. L., Mustard, J. F., Clark, R. N., Swayze, G. A., & Murchie, S. L. (2011). Evidence for low-grade metamorphism, hydrothermal alteration, and diagenesis on Mars from phyllosilicate mineral assemblages. *Clays and Clay Minerals*, *59*(4), 359–377. https://doi.org/10.1346/ccmn.2011.0590402
Ehlmann, B. L., Mustard, J. F., Murchie, S. L., Poulet, F., Bishop, J. L., Brown, A. J., et al. (2008). Orbital identification of carbonate-bearing rocks on Mars. *Science*, *322*(5909), 1828–1832. https://doi.org/10.1126/science.1164759
Falk, E. S., & Kelemen, P. B. (2015). Geochemistry and petrology of listvenite in the Samail ophiolite, Sultanate of Oman: Complete carbonation of peridotite during ophiolite emplacement. *Geochimica et Cosmochimica Acta*, *160*, 70–90. https://doi.org/10.1016/j.gca.2015.03.014
Frey, M., & Robinson, D. (2009). *Low-grade metamorphism*. John Wiley & Sons.
Gaffey, S. J. (1986). Spectral reflectance of carbonate minerals in the visible and near infrared (0.35-2.55 microns); calcite, aragonite, and dolomite. *American Mineralogist*, *71*(1–2), 151–162.
Glennie, K. W., Boeuf, M. G. A., Hughes-Clark, M. W., Moody-Stuart, M., Pilaar, W. F. H., & Reinhardt, B. M. (1973). Late cretaceous nappes in Oman mountains and their geologic evolution. *American Association of Petroleum Geologists Bulletin*, *57*, 5–27. https://doi.org/10.1306/819a4240-16c5-11d7-8645000102c1865d
Green, R. O., et al. (2015). Microimaging spectroscopy for the exploration of small bodies: First laboratory measurements of carbonaceous chondrite and HED meteorites and a proposed M6 instrument for in situ measurement. In: *46th Lunar and Planetary Science Conference*. Lunar and Planetary Institute. Abstract #2154.
Greenberger, R. N., Ehlmann, B. L., Osinski, G. R., Tornabene, L. L., & Green, R. O. (2020). Compositional heterogeneity of impact melt rocks at the Haughton impact structure, Canada: Implications for planetary processes and remote sensing. *Journal of Geophysical Research: Planets*, *125*, e2019JE006218. https://doi.org/10.1029/2019JE006218
Greenberger, R. N., Mustard, J. F., Ehlmann, B. L., Blaney, D. L., Cloutis, E. A., Wilson, J. H., et al. (2015). Imaging spectroscopy of geological samples and outcrops: Novel insights from microns to meters. *Geological Society of America Today*, *25*(12), 4–10. https://doi.org/10.1130/GSATG252A.1
Gregory, R. T., & Taylor, H. P., Jr. (1981). An Oxygen Isotope Profile in a Section of Cretaceous Oceanic Crust,Samail Ophiolite,Oman:Evidence for 180 Buffering of the Oceans by Deep (>5 km) Seawater-Hydrothermal Circulation at Mid-Ocean Ridges. *Journal of Geophysical Research*, *86*(B4), 2737–2755. https://doi.org/10.1029/jb086ib04p02737
Halls, C., & Zhao, R. (1995). Listwaenite and related rocks: Perspectives on terminology and mineralogy with reference to an occurrence at Cregganbaun, Co. Mayo, Republic of Ireland. *Mineralium Deposita*, *30*(3–4), 303–313. https://doi.org/10.1007/bf00196366
Hanghøj, K., Kelemen, P. B., Hassler, D., & Godard, M. (2010). Composition and genesis of depleted mantle peridotites from the Wadi Tayin massif, Oman ophiolite. Major and trace element geochemistry, and Os isotope and PGE systematics. *Journal of Petrology*, *51*, 206–227. https://doi.org/10.1093/petrology/egp077
Heylen, R., Burazerovic, D., & Scheunders, P. (2011). Fully constrained least squares spectral unmixing by simplex projection. *Geoscience and Remote Sensing, IEEE Transactions on*, *49*(11), 4112–4122. https://doi.org/10.1109/tgrs.2011.2155070

Hopson, C. A., Coleman, R. G., Gregory, R. T., Pallister, J. S., & Bailley, E. H. (1981). Geologic section through the Samail Ophiolite and associated rocks along the Muscat-Ibra transect, southeastern Oman Mountains. *Journal of Geophysical Research*, *86*, 2527–2544. https://doi.org/10.1029/jb086ib04p02527

Horgan, B. H. N., Anderson, R. B., Dromart, G., Amador, E. S., & Rice, M. S. (2020). The mineral diversity of Jezero crater: Evidence for possible lacustrine carbonates on Mars. *Icarus*, *339*, 113526. https://doi.org/10.1016/j.icarus.2019.113526

Hubas, C., Jesus, B., Passarelli, C., & Jeanthon, C. (2011). Tools providing new insight into coastal anoxygenic purple bacterial mats: Review and perspectives. *Research in Microbiology*, *162*(9), 858–868. https://doi.org/10.1016/j.resmic.2011.03.010

Hunt, G. R., Salisbury, J. W., & Lenhoff, C. J. (1970). Visible and near-infrared spectra of minerals and rocks: I silicate minerals. *Modern Geology*, *1*, 283–300.

Hynek, B. M., Beach, M., & Hoke, M. R. T. (2010). Updated global map of Martian valley networks and implications for climate and hydrologic processes. *Journal of Geophysical Research*, *115*(E9). https://doi.org/10.1029/2009je003548

Jakob, S., Zimmerman, R., & Gloaguen, R. (2017). The need for accurate geometric and radiometric corrections of drone-borne hyperspectral data for mineral exploration: MEPHySTo—A toolbox for pre-processing drone-borne hyperspectral data. *Remote Sensing*, *9*(1), 88. https://doi.org/10.3390/rs9010088

Kelemen, P. B., Evans, O., Ghiorso, M., Mustard, J., Ehlmann, B. L., & Spiegelman, M. (2020b). Carbonate in olivine-rich unit(s) on Mars may have formed at low P(H_2O). In: *51st Lunar and Planetary Science Conference Abstracts*, 1213.

Kelemen, P. B., & Matter, J. (2008). In situ carbonation of peridotite for CO_2 storage. *Proceedings of the National Academy of Sciences*, *105*(45), 17295–17300. https://doi.org/10.1073/pnas.0805794105

Kelemen, P. B., Matter, J. M., Teagle, D. A. H., & Coggon, J. A. (2020a). The Oman Drilling Science Teamand specific chapters therein. In: *Proceedings of the Oman drilling project*. International Ocean Discovery Program. https://doi.org/10.14379/Oman.ph1-2.proc.2020. Retrieved from http://publications.iodp.org/other/Oman/OmanDP.html

King, T. V. V., & Clark, R. N. (1989). Spectral characteristics of chlorites and Mg-serpentines using high-resolution reflectance spectroscopy. *Journal of Geophysical Research*, *94*(B10), 13997–14008. https://doi.org/10.1029/JB094iB10p13997

Koga, K., Kelemen, P. B., & Shimizu, N. (2001). Petrogenesis of the crust-mantle transition zone (MTZ) and the origin of lower crustal wehrlite in the Oman Ophiolite. *Geochemistry, Geophysics, Geosystems*. G-cubed)2000GC000132..

Kokaly, R. F., Clarkn, R. N., Swayze, G. A., Livo, K. E., Hoefen, T. M., Pearson, N. C., et al. (2017). *USGS spectral library version 7*. US Geological Survey.

Kokaly, R. F., Despain, D. G., Clarkn, R. N., & Livo, K. E. (2007). *Spectral analysis of absorption features for mapping vegetation cover and microbial communities in Yellowstone National Park using AVIRIS data*.

Lapotre, M. G., Ehlmann, B. L., Minson, S. E., Arvidson, R. E., Ayoub, F., Fraeman, A. A., et al. (2017). Compositional variations in sands of the Bagnold Dunes, Gale crater, Mars, from visible-shortwave infrared spectroscopy and comparison with ground truth from the Curiosity rover. *Journal of Geophysical Research: Planets*, *122*(12), 2489–2509. https://doi.org/10.1002/2016je005133

Leask, E. K., Ehlmann, B. L., Greenberger, R. N., Pinet, P., Daydou, Y., Ceuleneer, G., & Kelemen, P. (2021). *Tracing carbonate formation, serpentinization, and biological materials with micro-/meso-scale infrared imaging spectroscopy in a Mars analog system*. Samail ophiolite. https://doi.org/10.22002/D1.2028

Leask, E. L., & Ehlmann, B. L. (2016). Identifying and quantifying mineral abundance through VSWIR microimaging spectroscopy: A comparison to XRD and SEM. In: *IEEE transactions, IEEE 8th workshop on hyperspectral image and signal processing: Evolution in remote sensing* (pp. 215p–24). WHISPERS). https://doi.org/10.1109/WHISPERS.2016.8071774

Leask, E. L., & Ehlmann, B. L. (2017). *Identifying and Quantifying Mineral Abundance through VSWIR Microimaging Spectroscopy: A Comparison to XRD and SEM*. CaltechDATA. https://doi.org/10.22002/D1.222

Leleu, T., Chavagnac, V., Delacour, A., Noiriel, C., Ceuleneer, G., Aretz, M., et al. (2016). Travertine associated with hyperalkaline springs: Evaluation as a proxy for paleoenvironmental conditions and sequestration of atmospheric CO2. *Journal of Sedimentary Research*, *86*, 1328–1343. https://doi.org/10.2110/jsr.2016.79

Martin, P. E., Ehlmann, B. L., Thomas, N. H., Wiens, R. C., Hollis, J. J. R., Beegle, L. W., et al. (2020). Studies of a lacustrine-volcanic Mars analog field site with Mars-2020-like instruments. *Earth and Space Science*, *7*, e2019EA000720. https://doi.org/10.1029/2019EA000720

Menzel, M. D., Urai, J. L., de Obeso, J. C., Kotowski, A., Manning, C. E., Kelemen, P. B., et al. (2020). Brittle deformation of carbonated peridotite— Insights from listvenites of the Samail ophiolite (Oman Drilling Project Hole BT1B). *Journal of Geophysical Research: Solid Earth*, *125*, e2020JB020199. https://doi.org/10.1029/2020JB020199

Michalski, J. R., & Niles, P. B. (2010). Deep crustal carbonate rocks exposed by meteor impact on Mars. *Nature Geoscience*, *3*(11), 751–755. https://doi.org/10.1038/ngeo971

Monnier, C., Girardeau, J., Le Mée, L., & Polvé, M. (2006). Along-ridge petrological segmentation of the mantle in the Oman ophiolite. *Geochemistry, Geophysics, Geosystems*, *7*, Q11008. https://doi.org/10.1029/2006GC001320

Murchie, S., Arvidson, R., Bedini, P., Bibring, J.-P., Bishop, J., Boldt, P., et al. (2007). Compact reconnaissance imaging spectrometer for Mars (CRISM) on Mars reconnaissance orbiter (MRO). *Journal of Geophysical Research*, *112*(E5).

Murchie, S. L., Mustard, J. F., Ehlmann, B. L., Milliken, R.E., Bishop, J. L., Mckeown, N. K., et al. (2009). A synthesis of Martian aqueous mineralogy after 1 Mars year of observations from the Mars Reconnaissance Orbiter. *Journal of Geophysical Research*, *114*(E2). https://doi.org/10.1029/2009je003342

Mustard, J. F., & Pieters, C. M. (1989). Photometric phase functions of common geologic minerals and applications to quantitative analysis of mineral mixture reflectance spectra. *Journal of Geophysical Research: Solid Earth*, *94*(B10), 13619–13634. https://doi.org/10.1029/jb094ib10p13619

Nasir, S., Al Sayigh, A., Al Harthy, A., Al-Khirbash, S., Al-Jaaidi, O., Musllam, A., et al. (2007). Mineralogical and geochemical characterization of listwaenite from the Semail Ophiolite, Oman. *Chemie der Erde*, *67*, 213–228. https://doi.org/10.1016/j.chemer.2005.01.003

Neal, C., & Stanger, G. (1984). Calcium and magnesium hydroxide precipitation from alkaline groundwaters in Oman, and their significance to the process of serpentinization. *Mineralogical Magazine*, *48*(347), 237–241. https://doi.org/10.1180/minmag.1984.048.347.07

Neal, C., & Stanger, G. (1985). Past and present serpentinization of ultramafic rocks: An example from the Semail ophiolite nappe of northern Oman. In J. I. Drewer (Ed.), *The chemistry of weathering* (pp. 249–275). D. Reidel Publishing Company. https://doi.org/10.1007/978-94-009-5333-8_15

Niles, P. B., Catling, D. C., Berger, G., Chassefiere, E., Ehlmann, B. L., Michalski, J. R., et al. (2013). Geochemistry of carbonates on Mars: Implications for climate history and nature of aqueous environments. *Space Science Reviews*, *174*(1–4), 301–328. https://doi.org/10.1007/s11214-012-9940-y

Paukert, A. P., Matter, J. M., Kelemen, P. B., Shock, E. L., & Havig, J. R. (2012). Reaction path modeling of enhanced in situ CO2 mineralization for carbon sequestration in the peridotite of the Samail Ophiolite. *Sultanate of Oman: Chemical Geology*, *330–331*, 86–100. https://doi.org/10.1016/j.chemgeo.2012.08.013

Pelkey, S., Mustard, J. F., Murchie, S., Clancy, R. T., Wolff, M., Smith, M., et al. (2007). CRISM multispectral summary products: Parameterizing mineral diversity on Mars from reflectance. *Journal of Geophysical Research*, *112*(E8). https://doi.org/10.1029/2006je002831

Peterson, D. L., & Hubbard, G. (1992). *Scientific issues and potential remote-sensing requirements for plant biochemical content*.

Pieri, D. C. (1980). martian valleys: Morphology, distribution, age, and origin. *Science*, *210*(4472), 895–897. https://doi.org/10.1126/science.210.4472.895

Pilorget, C., & Bibring, J.-P. (2013). NIR reflectance hyperspectral microscopy for planetary science: Application to the MicrOmega instrument. *Planetary and Space Science*, *76*, 42–52. https://doi.org/10.1016/j.pss.2012.11.004

Pinet, P., Harris, J. F., Python, M., Ceuleneer, G., Launeau, P., Daydou, Y., et al. (2003). Hyperspectral remote sensing approach for rock surface mineralogy mapping in arid environment. In: *Proceedings IUGG XXXIII general assembly*. Sapporo (Japon).

Pinet, P., Clenet, H., Rosemberg, C., Ceuleneer, G., Heuripeau, F., Harris, E., et al. (2006). Mantle rock surface mineralogy mapping in arid environment from imaging spectroscopy: The case of the Maqsad peridotitic massif in Oman and implications for the spectroscopic study of exposed mafic units on Mars. In: *Proceedings of the Lunar and Planetary Science Conference, 37th*.

Pinet, P. C., & Chevrel, S. (1990). Spectral identification of geological units on the surface of Mars related to the presence of silicates from Earth-based near-infrared telescopic charge-coupled device imaging. *Journal of Geophysical Research*, *95*(14), 14435–14446. https://doi.org/10.1029/jb095ib09p14435

Pinet, P. C., Daydou, Y. D., Rospabé, M., Ceuleneer, G., Ehlmann, B. L., Leask, E., et al. (2017). Long distance hyperspectral imaging panorama over the dunitic transition zone/moho contact of the Oman ophiolite: In situ testing and scientific assessment of a new advanced sensor. In: *Lunar Planetary Science Conference* (Vol. 48th). Retrieved from https://www.hou.usra.edu/meetings/lpsc2017/eposter/1868.pdf

Pollack, J. B., Kasting, J. F., Richardson, S. M., & Poliakoff, K. (1987). The case for a wet, warm climate on early Mars. *Icarus*, *71*(2), 203–224. https://doi.org/10.1016/0019-1035(87)90147-3

Rempfert, K. R., Miller, H. M., Bompard, N., Nothaft, D., Matter, J. M., Kelemen, P., et al. (2017). Geological and geochemical controls on subsurface microbial life in the Samail Ophiolite, Oman. *Frontiers in Microbiology*, *8*, 56. https://doi.org/10.3389/fmicb.2017.00056

Rioux, M., Bowring, S., Kelemen, P., Gordon, S., Dudas, F., & Miller, R. (2012). Rapid crustal accretion and magma assimilation in the Oman-U.A.E. ophiolite : High precision U-Pb zircon geochronology of the gabbroic crust. *Journal of Geophysical Research*, *117*, B07201. https://doi.org/10.1029/2012JB009273

Rioux, M., Garber, J., Bauer, A., Bowring, S., Searle, M., Kelemen, P., & Hacker, B. (2016). Synchronous formation of the metamorphic sole and igneous crust of the Semail ophiolite: New constraints on the tectonic evolution during ophiolite formation from high-precision U-Pb zircon geochronology. *Earth and Planetary Science Letters*, *451*, 185–195. https://doi.org/10.1016/j.epsl.2016.06.051

Rospabé, M., Benoit, M., Ceuleneer, G., Hodel, F., & Kaczmarek, M.-A. (2018). Extreme geochemical variability through the duntic transition zone of the Oman ophiolite: Implications for melt/fluid-rock reactions at Moho level beneath oceanic spreading centers. *Geochimica et Cosmochimica Acta*, *234*, 1–23. https://doi.org/10.1016/j.gca.2018.05.012

Roy, R., Launeau, P., Carrere, V., Pinet, P., Ceuleneer, G., Clenet, H., Daydou, Y., et al. (2009). Geological mapping strategy using visible near-infrared–shortwave infrared hyperspectral remote sensing: Application to the Oman ophiolite (Sumail Massif). *Geochemistry, Geophysics, Geosystems*, *10*(2). https://doi.org/10.1029/2008gc002154

Schulte, M., Blake, D., Hoehler, T., & McCollom, T. (2006). Serpentinization and its implications for life on the early Earth and Mars. *Astrobiology*, *6*(2), 364–376. https://doi.org/10.1089/ast.2006.6.364

Searle, M., & Cox, J. (1999). Tectonic setting, origin, and obduction of the Oman ophiolite. *Geological Society of America Bulletin*, *111*(1), 104–122. https://doi.org/10.1130/0016-7606(1999)111<0104:tsoaoo>2.3.co;2

Stanger, G. (1985). Silicified serpentinite in the Semail nappe of Oman. *Lithos*, *18*, 13–22. https://doi.org/10.1016/0024-4937(85)90003-9

Stern, S., Bagenal, F., Ennico, K., Gladstone, G. R., Grundy, W. M., Mckinnon, W. B., Moore, J. M., et al. (2015). The Pluto system: Initial results from its exploration by New Horizons. *Science*, *350*(6258), aad1815.

Swayze, G., Clark, R. N., Kruse, F., Sutley, S., & Gallagher, A. (1992). *Ground-truthing AVIRIS mineral mapping at Cuprite*.

Tilton, G., Hopson, C. A., & Wright, J. E. (1981). Uranium-lead isotopic ages of the Samail ophiolite, Oman, with applications to Tethyan ocean ridge tectonics. *Journal of Geophysical Research: Solid Earth*, *86*(B4), 2763–2775. https://doi.org/10.1029/jb086ib04p02763

Van Gorp, B., Mouroulis, P., Blaney, D., Green, R. O., Ehlmann, B. L., & Rodriguez, J. I. (2014). Ultra-compact imaging spectrometer for remote, in situ, and microscopic planetary mineralogy. *Journal of Applied Remote Sensing*, *8*(1), 084988–084988. https://doi.org/10.1117/1.jrs.8.084988

Viviano-Beck, C. E., Seelos, F. P., Murchie, S. L., Kahn, E. G., Seelos, K. D., Taylor, H. W., et al. (2014). Revised CRISM spectral parameters and summary products based on the currently detected mineral diversity on Mars. *Journal of Geophysical Research: Planets*, *119*(6), 1403–1431. https://doi.org/10.1002/2014je004627

Web, R. *Reflectance experiment laboratory (RELAB) description and user's manual*.

Wessman, C. A. (1990). *Evaluation of canopy biochemistry Remote sensing of biosphere functioning* (pp. 135–156). Springer. https://doi.org/10.1007/978-1-4612-3302-2_7

White, A. J. R., Laukamp, C., Stokes, M. A., Legras, M., & Pejcic, B. (2017). Vibrational spectroscopy of epidote, pumpellyite and prehnite applied to low-grade regional metabasites. *Geochemistry: Exploration, Environment, Analysis*, *17*, 315–333.

Wilde, A., Simpson, L., & Hanna, S. (2002). Preliminary study of tertiary hydrothermal alteration and platinum deposition in the Oman ophiolite. *Journal of the Virtual Explorer*, *6*, 7–13.

Wray, J., Milliken, R. E., Dundas, C. M., Swayze, G. A., Andrews-Hanna, J. C., Baldridge, A. M., et al. (2011). Columbus crater and other possible groundwater-fed paleolakes of Terra Sirenum, Mars. *Journal of Geophysical Research: Planets*, *116*(E1). https://doi.org/10.1029/2010je003694